Reconstruction of $\delta^{13}C_{DIC}$ in the Atlantic Ocean: A Probabilistic Machine Learning Approach for Filling Historical Data Gaps

Hui Gao[1,2], Zelun Wu[1], Zhentao Sun[1], Diana Cai[3], Meibing Jin[4,5], Wei-Jun Cai[1*]

[1]School of Marine Science and Policy, University of Delaware, Newark, Delaware, USA.
[2]College of Chemistry and Environmental Science, Guangdong Ocean University, Zhanjiang, China.
[3]Center for Computational Mathematics, Flatiron Institute, New York, New York, USA.
[4]School of Marine Sciences, Nanjing University of Information Science and Technology, Nanjing, China.
[5]International Arctic Research Center, University of Alaska Fairbanks, Fairbanks, Alaska, USA.

Correspondence to: Wei-Jun Cai (wcai@udel.edu)

Abstract. Stable carbon isotope composition of marine dissolved inorganic carbon (DIC), $\delta^{13}C_{DIC}$, is a valuable tracer for oceanic carbon cycling. However, its observational coverage remains much sparser than that of DIC and other physical or biogeochemical variables, limiting its full potential. Here, we reconstruct $\delta^{13}C_{DIC}$ in the Atlantic Ocean using a probabilistic machine learning framework, Gaussian Process Regression (GPR). We compiled data from 51 historical cruises, including a high-resolution 2023 A16N transect, and applied secondary quality control via crossover analysis, retaining 37 cruises for model training, validation, and testing. The trained GPR model achieved an average bias of −0.007 ± 0.082 ‰ and an overall uncertainty of 0.11 ‰, arising from measurement (0.07 ‰), mapping (0.08 ‰), and input-variable (0.009 ‰) errors. To address validation limitations related to sparse observation, we further supplemented this work with numerical model-based validation (Claret et al., 2021), confirming the GPR model's robustness in $\delta^{13}C_{DIC}$ reconstruction ~~($R^2 > 0.99$ and RMSE < 0.015‰)~~. Using the GLODAPv2.2023 Atlantic dataset as predictors, the reconstruction expanded the number of acceptable $\delta^{13}C_{DIC}$ samples by a factor of 7.65, from 8,941 to 68,435 across the Atlantic basins. The resulting dataset markedly improves the spatial resolution in longitude, latitude, and depth, and provides enhanced temporal continuity over the past four decades, offering great advantages in decadal trend assessment. Compared to the sparse original measurements, the reconstruction also reduces spatial discontinuities and reveals finer vertical structures consistent with other high-resolution biogeochemical observations. This reconstructed $\delta^{13}C_{DIC}$ dataset provides new opportunities to resolve regional carbon cycle dynamics, validate Earth system models, refine estimates of oceanic carbon uptake on at least decadal timescale, and extend climate reanalysis records. The data are publicly accessible at the data repository Zenodo under the following DOI: https://doi.org/10.5281/zenodo.18481145 ~~https://doi.org/10.5281/zenodo.16907402~~ (Gao et al., 2025).

1 Introduction

The stable carbon isotope ratio has been widely applied as a tracer in marine carbon research, providing valuable insights into various processes within the oceanic carbon system. It is expressed via the standard delta notation: $\delta^{13}C = ((^{13}C/^{12}C)_{sample}/(^{13}C/^{12}C)_{standard}-1)\times10^3$, referenced against the international standard, the Vienna Pee Dee Belemnite ([V]-PDB) fossil. Specifically, the $\delta^{13}C$ of dissolved inorganic carbon (DIC), denoted as $\delta^{13}C_{DIC}$ (expressed in per mil, ‰), has proven instrumental in studies encompassing estimating rates of biological production in surface ocean mixed layer (Quay et al., 2003, 2009; Yang et al., 2019), quantifying anthropogenic carbon inputs and accumulations in ocean basins (Quay et al., 1992, 2003, 2007, 2017; Körtzinger et al., 2003; Olsen and Ninnemann, 2010; Racapé et al., 2013), and validating earth system models (Sonnerup and Quay, 2012; Schmittner et al., 2013; Liu et al., 2021; Claret et al., 2021), making it an indispensable parameter in understanding the complexities of the marine carbon cycle.

Measurements of $\delta^{13}C_{DIC}$ in the ocean trace their roots to the mid-20th century, with significant advancements occurring in the 1970s and 1980s due to the development of more precise mass spectrometry techniques. A pivotal moment in marine isotope research came with Kroopnick's comprehensive analyses of $\delta^{13}C_{DIC}$ distribution in the Atlantic Ocean (Kroopnick, 1980) and globally (Kroopnick, 1985), which provided critical insights into isotopic patterns across the oceans. Over subsequent decades, observational $\delta^{13}C_{DIC}$ data and their biogeochemical interpretation continue to increase (Gruber et al., 1999; Quay et al., 2003; Quay et al. 2017; Schmittner et al., 2013). The creation of databases such as Global Ocean Data Analysis Project (GLODAP) further enhanced access to $\delta^{13}C_{DIC}$ data and other carbon-related parameters (Olsen et al., 2016). However, unlike other carbon datasets such as DIC and total alkalinity (TA), $\delta^{13}C_{DIC}$ lacked secondary quality control until Becker et al. (2016) introduced an internally consistent $\delta^{13}C_{DIC}$ dataset for the North Atlantic, marking a significant step in addressing biases and improving data reliability. But still, unlike other carbon datasets, $\delta^{13}C_{DIC}$ lacks necessary sufficiently high spatial resolution for it to be effective in ocean carbon cycle research and as a tracer for anthropogenic carbon accumulation in the ocean.

Traditionally, $\delta^{13}C_{DIC}$ data have been acquired by preserving and transporting seawater samples to shore-based laboratories for analysis via Isotope Ratio Mass Spectrometry (IRMS). Although the IRMS approach is highly precise and accurate, it is labor-intensive and unsuitable for at-sea analysis, and incapable of measuring precise DIC concentrations concurrently. These limitations have significantly restricted the collection of $\delta^{13}C_{DIC}$ data, impeding efforts to characterize spatiotemporal variabilities and long-term trends of $\delta^{13}C_{DIC}$. For example, in the Atlantic Ocean, only 6,820 $\delta^{13}C_{DIC}$ measurements were collected across 32 cruises over 40 years, averaging just 213 samples per cruise (Becker et al., 2016). Specifically, along the A16N transect, approximately 500 samples were collected during the 1993 and 2013 cruises and only 38 surface water samples were collected during the 2003 cruise for land-based $\delta^{13}C_{DIC}$ analysis, showing a stark contrast to the fact that about 3,000 DIC samples were analysed at sea per cruise. To overcome this severe bottleneck, the Cai Lab has developed a precise, rapid, and sea-going suitable $\delta^{13}C_{DIC}$ analytical method with a precision of better than ±0.05 ‰ based on the Cavity Ring-Down

Spectroscopy (CRDS) stable carbon isotope analyzer, G2131-*i* (Su et al., 2019; Deng et al., 2022; Sun et al., 2024; Sun et al., 2025). This method has been extensively tested during several recent observations and studies. During a long (58-day) ocean cruise along A16N in 2023, approximately 3,500 $\delta^{13}C_{DIC}$ samples were collected, with ~3000 samples analysed at sea, alongside DIC observations. This progress has significantly surpassed the historical A16N datasets (Sun et al., 2025).

Despite extensive field data collection efforts, observations of $\delta^{13}C_{DIC}$ remain sparse compared to other inorganic carbon chemistry variables (e.g., DIC and TA). The distribution and variations of inorganic carbon chemistry within water masses are governed by both the source-water properties and physical and biogeochemical processes, resulting in region-specific stoichiometric relationships among inorganic carbon variables. These relationships are typically nonlinear and exhibit spatial and temporal variability, making it challenging to determine general distribution patterns. In recent decades, advancements in machine learning techniques coupled with accumulated observational data have facilitated numerous studies that interpolate inorganic carbon chemistry variables, ~~in particular~~particularly the partial pressure of CO_2 (pCO_2) due to its relatively high spatial coverage, from satellite data and reanalysis products (e.g., Landschützer et al., 2016; Gregor & Gruber, 2021; Roobert et al., 2024; Wu et al., 2025). These methodological developments present a promising opportunity to investigate the potential for deriving $\delta^{13}C_{DIC}$ data from more abundantly measured variables.

Given the limited and fragmented $\delta^{13}C_{DIC}$ dataset compared to other parameters such as DIC, and to fully utilize the $\delta^{13}C_{DIC}$ tracer approach for quantifying anthropogenic CO_2 uptake by the ocean (Quay et al., 2017), the rate of ocean biological production (Esposito et al., 2019; Quay et al., 2009, 2020, 2023), and carbon cycling across the land-ocean interface (Alling et al., 2012; Kwon et al., 2021; Samanta et al., 2015), this study aims to reconstruct a high-resolution $\delta^{13}C_{DIC}$ dataset for the Atlantic Ocean using Gaussian Process Regression (GPR), a probabilistic machine-learning approach capable of capturing nonlinear relationships and spatial-temporal variability. This reconstruction integrates historical $\delta^{13}C_{DIC}$ observations in the Atlantic Ocean with new high-resolution data collected along the A16N transect in 2023 (Sun et al., 2025), and the product of GLODAPv2.2023 (Lauvset et al., 2024). The final product consists of two components with comprehensive uncertainty analysis: 1) a quality-controlled $\delta^{13}C_{DIC}$ observational dataset compiled from 51 cruises with a crossover analysis using standardized protocols, and 2) a machine learning-reconstructed $\delta^{13}C_{DIC}$ dataset derived from other inorganic carbon chemistry variables. The structure of this study is as follows: **Section 2** describes the datasets used, the secondary quality control of $\delta^{13}C_{DIC}$, and the methodology for reconstructing the $\delta^{13}C_{DIC}$ dataset. **Section 3** evaluates the accuracy, performance, and applicability of the reconstructed $\delta^{13}C_{DIC}$ dataset in resolving its spatial and temporal distribution. **Section 4** presents the conclusions. **Sections 5 and 6** provide access the dataset, the codes used for its generation, and the figures presented in this study. The Appendix provides additional evaluation and validation by applying the same ML approach to numerical model outputs.

2 Data and Methods

2.1 Data collection

2.1.1 Historical $\delta^{13}C_{DIC}$ Data Collection

In the Atlantic Ocean, $\delta^{13}C_{DIC}$ data were compiled from several international research initiatives, including GLODAP, Ocean Carbon and Acidification Data System (OCADS), Climate and Ocean Variability, Predictability, and Change (CLIVAR), Carbon Hydrographic Data Office (CCHDO) and the internally consistent dataset of $\delta^{13}C_{DIC}$ in the North Atlantic Ocean (NAC13v1, Becker et al., 2016). Notably, most cruises in the final compiled dataset are sourced from GLODAP. Cruises from the other aforementioned databases were only included to supplement those not covered by GLODAP, and no duplicate cruises were counted to ensure each unique cruise is represented exactly once. From the original dataset published by Becker et al. (2016), we excluded four cruises: 35TH20060521, 74JC20120601, 74DI20140606, and OMEX1NA, due to missing essential corresponding parameters, i.e., variables used for model training. The remaining cruises, including those from other sources and the 28 cruises retained from Becker et al. (2016), comprise a total of 51 cruises, covering 369 stations and 15,225 $\delta^{13}C_{DIC}$ samples (**Fig. 1 and Table 1**). To ensure internal consistency, samples from depths greater than 2,000 m were selected for crossover analysis. Specifically, deep waters below 2000 m in the South Atlantic Ocean are most likely not impacted by anthropogenic carbon (i.e., Gao et al., 2022, 2024), supporting this threshold. In contrast, North Atlantic Deep Water (NADW) formation may drive small but measurable decadal anthropogenic carbon changes even below 2000 m. However, Becker et al. (2016) showed that restricting analysis to depths > 2000 m effectively reduces cruise offset variability in variable North Atlantic regions (e.g., Labrador Sea, Nordic Seas), further validating our 2000 m threshold for the Atlantic. This criterion resulted in 3,772 samples from 305 stations deeper than 2,000 m (highlighted as red points in **Fig. 1a**). The temporal and latitudinal distributions of the $\delta^{13}C_{DIC}$ data are illustrated in **Fig. 1b and 1c, respectively**. These datasets span from 1981 to 2023, with the most comprehensive annual $\delta^{13}C_{DIC}$ sampling occurring along A16N in 2023 (**Fig. 1b**). However, the sampling is spatially and temporally uneven, that is, data are sparse in certain years and latitudes, which underscores the need for an approach capable of generating robust predictions and uncertainty estimates in poorly sampled regions, such as the GPR method applied in this study. In particular, ~~geographically,~~ the majority of samples are concentrated in the North Atlantic, particularly between latitudes 25° N and 60° N (**Fig. 1c**).

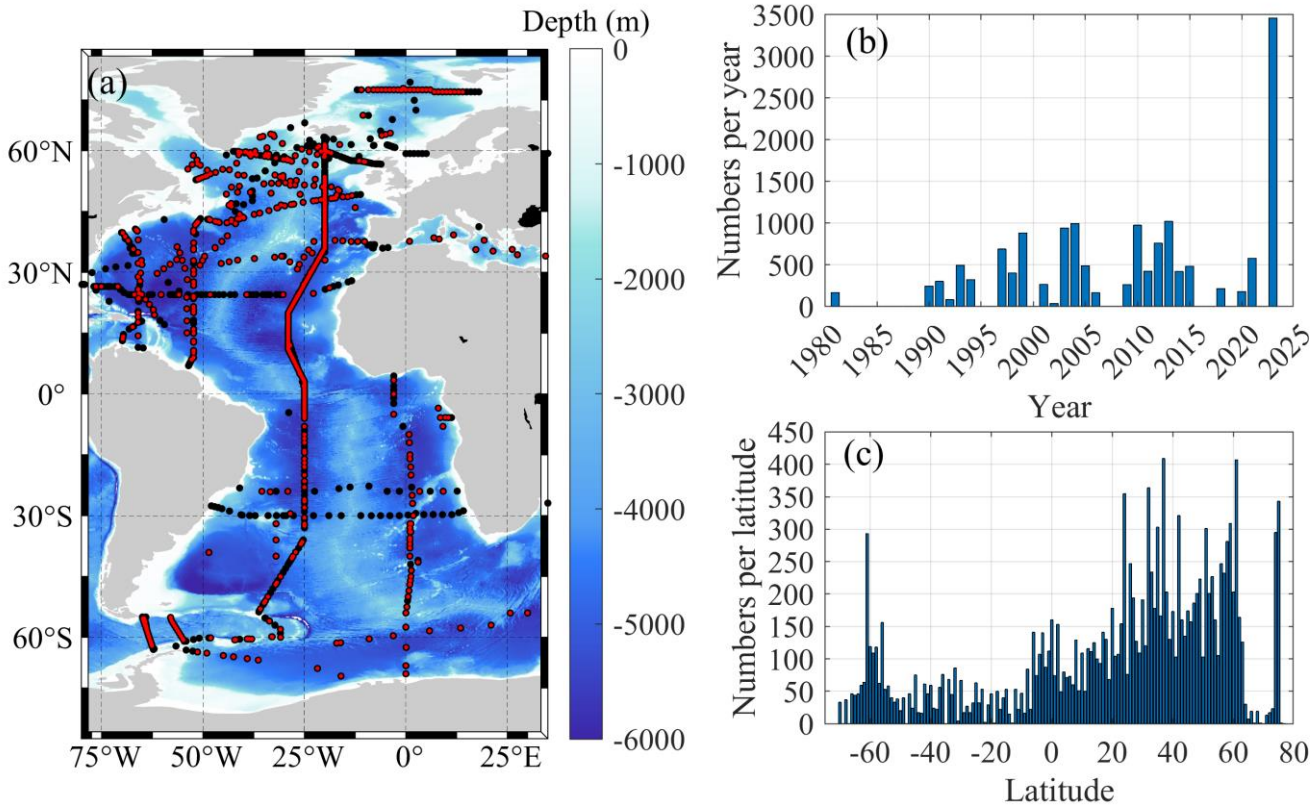

Figure 1. Overview of the collected $\delta^{13}C_{DIC}$ data. (a) Map of all stations with $\delta^{13}C_{DIC}$ data in the Atlantic Ocean, with stations containing samples deeper than 2,000 m highlighted in red. (b) Temporal distribution of $\delta^{13}C_{DIC}$ data, organized by year of collection. (c) Total number of $\delta^{13}C_{DIC}$ samples aggregated by each degree of latitude.

Table 1. Information about Cruises that contains $\delta^{13}C_{DIC}$, and adjustment for each cruise.

Cruse No.	Expocode	Cruise Name	Dates	C13 PIs	Adjustments from Becker et al. (2016)	Additional Adjustments
1	06AQ20101128	A12 SR04 ANT XXVII/2	2010-11-28/2011-02-05	R. Key, A. McNichol, S. Heuven	/	0
2	06MT19941012	WOCE A02 06MT30_2 CARINA	1994-10-12/1994-11-12	A. Körtzinger, H. Erlenkeuser	−0.07	0

3	06MT19970515	WOCE AR12 AR24 06MT39_2	1997-05-15/1997-06-07	A. Körtzinger, H. Erlenkeuser	0	0
4	06MT19970611	A02 06MT39_3	1997-06-11/1997-07-03	A. Körtzinger, H. Erlenkeuser	0	0
5	06MT19970707	WOCE AR05 AR07 AR07W 06MT39_4	1997-07-07/1997-08-07	A. Körtzinger, H. Erlenkeuser	0	0.05
6	06MT19970815	WOCE AR07E 06MT39_5	1997-08-14/1997-09-09	A. Körtzinger, H. Erlenkeuser	0	0.05
7	06MT19990610	06MT199906 06MT452 06MT45_2	1999-06-10/1999-07-09	A. Körtzinger, H. Erlenkeuser	−0.20	0
8	06MT19990711	AR07 AR07W 06MT45_3	1999-07-10/1999-08-11	A. Körtzinger, H. Erlenkeuser	−0.20	0
9	06MT20010507	A02 CARINA SFB 460;	2001-05-07/2001-05-31	A. Körtzinger, H. Erlenkeuser	−0.30	0
10	06MT20030723	CARINA SFB 460;	2003-07-24/2003-08-26	A. Körtzinger, H. Erlenkeuser	−0.15	0
11	06MT20040311	CARINA TTO A2 TTO_NAS_2004	2004-03-11/2004-04-13	D. W. R. Wallace, H. Erlenkeuser	0.10	0.03
12	06MT20110405	M84_3 06ME20110405 MT84_3 Mediterranean Sea	2011-04-05/2011-04-28	T. Tanhua, G. Schnaller	/	NC
13	18DL20150710	ArcticNet1502	2015-07-10 / 2015-08-20	A. Mucci	/	NC
14	29GD20120910	(EUROFLEETS) Iberia-Forams	2012-09-10/2012-09-15	A.Voelker	/	NC
15	316N19810401, 316N19810416, 316N19810516, 316N19810619, 316N19810721, 316N19810821, 316N19810923	TTO-NAS	1981-04-01 / 1981-10-19	C. D. Keeling, P. Guenther	0	0
16	316N19970717	WOCE A20	1997-07-17/1997-08-10	R. Key	−0.05	0
17	316N19970815	WOCE A22	1997-08-15/1997-09-03	R. Key	NC	0.05

18	316N20030922	A20_2003	2003-09-22/2003-10-20	R. Key, P. Quay	NC	NC
19	316N20031023	A22_2003	2003-10-23/2003-11-13	R. Key, P. Quay	NC	NC
20	33AT20120419	A20_2012	2012-04-19/2012-05-15	R.Key, A.Mcnichol;	/	0
21	33AT20120324	A22_2012	2012-03-24/2012-04-17	R.Key, A.McNichol	/	0
22	33LG20060321	A21_2006 LMG200603	2006-03-21/2006-04-04	T.Guilderson, P.Quay	/	NC
23	33LG20090916	A21_2009 LMG200909	2009-09-16/2009-10-09	T.Guilderson, P.Quay	/	NC
24	33MW19910711	A16S SATL-91 OACES91	1991-07-11/1991-08-05	P. Quay, R. Key	0	0.04
25	33MW19930704	A16N AR21 OACES93 NATL-93	1993-07-04/1993-08-30	P. Quay, R. Key	C	C
26	33RO19980123	A05 AR01	1998-01-23/1998-02-24	R. Key, P. Quay	NC	0.03
27	33RO20030604	A16N_2003	2003-06-04/2003-08-11	A. McNichol	/	NC
28	33RO20050111	A16S A23	2005-01-11/2005-02-24	A. McNichol	/	−0.10
29	33RO20100308	A13.5	2010-03-08/2010-04-18	R. Key, A. McNichol	/	0
30	33RO20110926	A10	2011-09-26/2011-10-31	A. Foreman, A. Coppola	/	NC
31	33RO20130803	A16N_2013	2013-08-03/2013-10-03	A. McNichol	/	0
32	33RO20131223	A16S A23	2013-12-23/2014-02-04	A. McNichol, R. Key	/	0
33	33RO20200321	A12 A13.5	2020-03-21/2020-04-17	W-J. Cai	/	0.07
34	33RO20230306	A16N_2023, Leg 1	2023-03-06/2023-04-07	W-J. Cai	/	0

35	33RO20230413	A16N_2023, Leg 2	2023-04-13/2023-05-09	W-J. Cai	/	0
36	35A320031214	BIOZAIRE_III	2003-12-14/2004-01-07	A. Vangriesheim	/	NC
37	35TH20020611	Ovide02 A25	2002-06-10/2002-07-12	H. Mercier	0.25	0
38	49NZ20031106	A10	2003-11-06/2003-12-05	Y. Kumamoto	/	NC
39	58GS20030922	GO-SHIP A75N	2003-09-22 / 2003-10-13	A. Olsen	NC	0
40	58GS20130717	CLIVAR_75N_2013	2013-07-17 / 2013-07-30	A. Olsen	/	0
41	58GS20150410	A01 AR07E_2015	2015-04-10/2015-04-26	A. Olsen & U. Ninnemann	/	0.18
42	58JH19920712	CARINA WOCE AR18b	1992-07-12 / 1992-07-28	R. Nydal	NC	0
43	58JH19940723	CARINA WOCE AR18d	1994-07-23 / 1994-08-16	R. Nydal	NC	0
44	64TR19900417	CARINA A16N	1990-04-17 / 1990-05-31	S. Wijma	poor	−0.76
45	740H20081226	A12 A21	2008-12-26/2009-01-30	W. Jenkins	/	0
46	740H20180228	A9.5 A10 A09	2018-02-28/2018-04-10	H. Graven	/	NC
47	74DI20120731	EEL_2012_D379 JR271_D379_2012	2012-07-31 /2012-08-17	A. M. Griffiths, M. P. Humphreys, E. P. Achterberg	0	0
48	74JC20100319	A21 A23	2010-03-19/2010-04-24	W.Jenkins	/	0
49	74JC20181103	SR01B	2018-11-03/2018-11-22	R.Key, A. McNichol	/	NC
50	325020210316	A20_2021	2021-03-16/2021-04-16	R. Sonnerup, R. Hansman	/	0
51	325020210420	A22_2021	2021-04-20/2021-05-16	R. Sonnerup, R. Hansman	/	0

Note: NC denotes cruises that were not considered for the adjustment due to the absence of statistically significant crossovers. The core cruise, identified as the reference, is marked with a "C."

2.1.2 $\delta^{13}C_{DIC}$ Data Collection Along A16N in 2023

The A16N cruise in 2023 achieved extensive collection and high-resolution analysis of $\delta^{13}C_{DIC}$ and DIC datasets over two legs using onboard analytical techniques. Samples were collected from CTD rosette bottles into 250 mL borosilicate glass bottles following PICES best practices, preserved with $HgCl_2$ to prevent biological activity, and sealed to prevent gas exchange. Analytical measurements were conducted onboard using two coupled systems comprising a CO_2 extraction device (AS-D1 $\delta^{13}C_{DIC}$ Analyzer) and a CRDS (Picarro G2131-i), which simultaneously measured DIC concentrations and $\delta^{13}C_{DIC}$ values with high precision. Quality control measures included frequent calibration using CRMs and homemade standards verified by IRMS, ensuring high data reliability with deviations mostly within ±0.03 ‰ for $\delta^{13}C_{DIC}$ (Sun et al., 2025).

2.2 Standardized Protocols for Crossover analysis

Secondary quality control (QC) of $\delta^{13}C_{DIC}$ data through crossover analysis ensures consistency across multi-cruise datasets (Becker et al., 2016; Tanhua et al., 2010; Lauvset & Tanhua, 2015). The analysis involves compiling data from overlapping regions, identifying crossover points within 222 km, and comparing $\delta^{13}C_{DIC}$ profiles in deep waters (> 2,000 m) where variability is minimal. Profiles are interpolated to standard depths or density. In this study, we adopted the density-based interpolation: standard sigma4 surfaces (potential density referenced to 4000 m) are generated at 0.05-unit intervals, covering all observed densities, based on the interpolated density profile of the deepest station, following the workflows presented in Lauvset & Tanhua (2015). Mean offsets between overlapping profiles at the selected standard densities are calculated. Detailed workflows were. Systematic biases are identified using least squares minimization, and adjustments are proposed to align datasets without erasing real temporal or spatial trends. Adjustments are validated against known regional patterns and applied only if they reduce discrepancies to within the measurement uncertainty. All steps and corrections are documented to ensure transparency, resulting in reliable $\delta^{13}C_{DIC}$ datasets for carbon cycle analysis. Building on the NAC13v1 dataset provided by Becker et al. (2016), we propose additional adjustment recommendations for these cruises (**Table 1**). Given that cruise 64TR19900417 crossovers with cruise 33MW19930704, 06MT20040311, 33RO20130803, 33RO20230413, showing a very high mean offset and standard deviation -0.76 ± 0.23 ‰, and its $\delta^{13}C_{DIC}$ data is marked as NaN (missing values) in the NAC13v1 dataset, it is excluded from our analysis. After applying additional adjustments, the $\delta^{13}C_{DIC}$ data for the remaining 37 cruises exhibit high internal consistency. These 37 cruises do not include 13 cruises without deep-water crossover stations (Table 1) and cruise 64TR19900417, which were excluded to ensure data reliability as their uncertainties cannot be objectively quantified. Collectively, these excluded cruises accounted for less than 3 % of total $\delta^{13}C_{DIC}$ measurements. The internal accuracy of the adjusted $\delta^{13}C_{DIC}$ is determined to be -4.15×10^{-5} ‰ based on the calculation from Tanhua et al. (2010) and Becker et al. (2016). Finally, a total of 11,950 samples are used to train and test the model (**Fig. 2**). These samples were selected

based on the quality flags of the relevant variables, where only data marked with quality flag values of 2 (acceptable measurement) or 6 (median of replicate measurements) were included, ensuring that the dataset is reliable and suitable for model development.

2.3 Model design

Predicting $\delta^{13}C_{DIC}$ in the ocean requires a method that can handle complex, highly nonlinear relationships and provide reliable uncertainty estimates for scientific interpretation. GPR (Seeger, 2004; Rasmussen & Williams, 2006) is particularly well suited to this task. As a non-parametric, probabilistic model, GPR not only produces point predictions but also quantifies uncertainty through credible intervals around the estimates. The versatility of GPR arises from its kernel function, which allows prior knowledge about the expected smoothness or variability of the $\delta^{13}C_{DIC}$-environment relationship to be incorporated into the model, making GPR a powerful tool for robust predictions in oceanographic applications.

We employed GPR with a Matern 5/2 kernel as the primary method for all subsequent $\delta^{13}C_{DIC}$ reconstructions, as it offers unique advantages tailored to addressing the core challenges of $\delta^{13}C_{DIC}$ data. The Matern class of kernels control function smoothness through its smoothness parameter. Specifically, the 5/2 kernel yields functions that are smooth yet not overly restrictive, offering a balanced representation that aligns well with the expected variability of many data sets. Thus, it is expected to provide a balanced representation aligned with the physical variability of $\delta^{13}C_{DIC}$ in the ocean. Compared with the widely used squared exponential kernel, which assumes infinitely differentiable, and often unrealistically smooth functions, the Matern 5/2 kernel allows for more plausible modeling of natural variability driven by ocean physical and biogeochemical processes such as mixing, air-sea CO_2 exchange, and biological productivity. As a Bayesian non-parametric model, GPR also inherently balances model complexity and data fit to avoid overfitting to sparse, noisy observations, a critical benefit given the small sample sizes of many cruises and uneven spatial-temporal coverage in our dataset.

To evaluate this approach's performance, ~~we compared~~ the Matern 5/2 GPR was compared with a suite of alternative regression models, including GPR with other kernels, as well as additional baselines such as neural networks, support vector regression, and decision trees. A rigorous validation framework that balances robustness, feasibility, and adherence to synoptic cruise data characteristics was designed to underpin this comparison. Specifically, the dataset was randomly split into a training set (80%) and a validation set (20%), with model training and hyperparameter tuning performed using 10-fold cross-validation within the training set to mitigate overfitting. An independent test set was reserved for final performance evaluation, selected to ensure no overlap with the training/validation set in cruises, spatial regions, or temporal coverage. Our preference for random splitting (over cruise-separated k-fold cross-validation) initially stemmed from concerns that cruise-separated splitting would cause imbalanced folds, given the small sample sizes of many of the 51 cruises, which could lead to unstable hyperparameter tuning and biased results. Additionally, random splitting preserves the natural spatiotemporal variability of $\delta^{13}C_{DIC}$, tuning the model

to generalize across diverse oceanic conditions rather than overfitting to specific cruises. This core validation framework aligns with established practices for sparse oceanographic datasets (Lima et al., 2023; Regier et al., 2023; Wu et al., 2025).

To further enhance the statistical robustness of performance metrics and address the concern of synoptic cruise data characteristics, we additionally implemented a cruise-separated 5-fold cross-validation. To address the small sample sizes of some cruises, cruises were allocated to folds using an iterative balancing procedure that minimizeds disparities in total sample size across foldsGiven the small sample sizes of many cruises, a greedy algorithm was adopted to group cruises into 5 folds, prioritizing approximately comparable total sample size per fold (rather than equal number of cruises per fold) to avoid biased results from imbalanced folds. Specifically, Eeach cruise was assigned to the fold with the smallest current sample size, resulting in fold sample sizes ranging from 1836 to 2718 samples (6–8 cruises per fold). To eliminate data leakage, standardization was performed independently for each fold using only the fold's training subset, ensuring the validity of cross-validation results.

To clarify the division of labor between the two cross-validation strategies, the 10-fold cross-validation was retained exclusively for hyperparameter tuning, while the cruise-separated 5-fold cross-validation focused on evaluating robust performance across synoptic cruise units. Predictive performance for all models was assessed using the Root Mean Squared Error (RMSE) and the coefficient of determination (R^2), computed separately for the validation and test sets. Among all tested models, including GPR with the squared exponential and other kernels (Table 2), the Matern 5/2 GPR achieved the best predictive performance (lowest RMSE and highest R^2) on both the validation set and the independent test set, while also providing meaningful uncertainty estimates, confirming its superiority for subsequent analysis.

This comparison was conducted alongside the implementation of 10-fold cross-validation within the training set, and the Matern 5/2 GPR achieved the best predictive performance among all tested models including GPR with the squared exponential and other kernels (Table 2). It yielded the lowest Root Mean Squared Error (RMSE) and the highest coefficient of determination (R^2) in this process and also provided meaningful uncertainty estimates, confirming its superiority for subsequent analysis. Among all tested models, including GPR with the squared exponential and other kernels (Table 2), GPR with the Matern 5/2 kernel achieved the best predictive performance (lowest RMSE and highest R^2) on the validation set as well as the independent test set, while also providing meaningful uncertainty estimates.

A rigorous validation framework that balances robustness, feasibility, and adherence to synoptic cruise data characteristics was designed. Specifically, For all regression models, the dataset was randomly split into a training set (80%) and a validation set (20%), with model training and hyperparameter tuning performed using 10-fold cross-validation within the training set to mitigate overfitting. An independent test set was reserved for final performance evaluation, selected to ensure no overlap with the training/validation set in cruises, spatial regions, or temporal coverage.

~~To further enhance the statistical robustness of performance metrics and address the concern of synoptic cruise data characteristics, we additionally implemented a cruise-separated 5-fold cross-validation. Given the small sample sizes of many cruises, a greedy algorithm was adopted to group cruises into 5 folds, prioritizing approximately comparable total sample size per fold (rather than equal number of cruises per fold) to avoid biased results from imbalanced folds. Each cruise was assigned to the fold with the smallest current sample size, resulting in fold sample sizes ranging from 1836 to 2718 samples (6–8 cruises per fold). To eliminate data leakage, standardization was performed independently for each fold using only the fold's training subset, ensuring the validity of cross-validation results. An independent test set was reserved for final performance evaluation, selected to ensure no overlap with the training/validation set in cruises, spatial regions, or temporal coverage. Our initial preference for random splitting (over cruise-separated k-fold) stemmed from concerns that cruise-separated splitting would cause imbalanced folds (due to small cruise sample sizes), which could lead to unstable hyperparameter tuning and biased results. The supplementary cruise-separated 5-fold cross-validation enabled by greedy grouping for sample size balance, effectively addressed this concern, serving as a critical complement to assess the model's stability across different cruise combinations. To clarify the division of labor, the 10-fold cross-validation was retained exclusively for hyperparameter tuning, while the cruise-separated 5-fold cross-validation focused on evaluating robust performance across synoptic cruise units. We opted for random splitting over cruise-separated k-fold cross-validation to balance robustness and feasibility as many of the 51 cruises have small sample sizes, and cruise separated splitting would cause imbalanced folds, leading to unstable hyperparameter tuning and biased results. Furthermore, Rrandom splitting also preserves natural spatiotemporal variability of $\delta^{13}C_{DIC}$, tuning the model to generalize across diverse oceanic conditions rather than overfitting to specific cruises. This validation framework aligns with established practices for sparse oceanographic datasets (Lima et al., 2023; Regier et al., 2023; Wu et al., 2025). Predictive performance was assessed using the Root Mean Squared Error (RMSE) and the coefficient of determination (R^2), computed separately for the validation and test sets. Among all tested models, including GPR with the squared exponential and other kernels (Table 2), GPR with the Matern 5/2 kernel achieved the best predictive performance (lowest RMSE and highest R^2) on the validation set as well as the independent test set, while also providing meaningful uncertainty estimates.~~

Table 2. Selection of machine-learning models based on Root Mean Squared Error (RMSE), and the coefficient of determination (R^2).

Model Name	RMSE (Validation)	R^2 (Validation)	RMSE (Test)	R^2 (Test)
Matern 5/2 Gaussian Process Regression	0.084	0.92	0.078	0.95
Rational Quadratic Gaussian Process Regression	0.084	0.92	0.081	0.95
Exponential Gaussian Process Regression	0.084	0.92	0.079	0.95
Squared Exponential Gaussian Process Regression	0.085	0.91	0.082	0.95
Wide Neural Network	0.089	0.90	0.136	0.86
Ensemble Bagged Trees	0.090	0.90	0.114	0.90
Medium Gaussian SVM	0.093	0.90	0.071	0.96

SVM Kernel	0.095	0.89	0.141	0.85
Medium Neural Network	0.094	0.89	0.091	0.94
Least Squares Regression Kernel	0.099	0.88	0.106	0.92
Bilayered Neural Network	0.104	0.87	0.093	0.94
Fine Gaussian SVM	0.105	0.87	0.258	0.50
Narrow Neural Network	0.106	0.86	0.097	0.93
Medium Tree	0.106	0.86	0.142	0.85
Fine Tree	0.108	0.86	0.144	0.84
Trilayered Neural Network	0.097	0.88	0.086	0.94
Coarse Tree	0.117	0.83	0.122	0.89
Ensemble Boosted Trees	0.119	0.83	0.163	0.80
Coarse Gaussian SVM	0.123	0.82	0.113	0.90
Stepwise Linear Regression	0.109	0.86	0.095	0.93
Interactions Linear Regression	0.109	0.85	0.099	0.93
Quadratic SVM	0.109	0.86	0.082	0.95
Efficient Linear Least Squares	0.154	0.71	0.179	0.76
Efficient Linear SVM	0.157	0.70	0.203	0.69
Linear SVM	0.156	0.70	0.201	0.70
Robust Linear Regression	0.157	0.70	0.208	0.68
Cubic SVM	0.094	0.89	0.078	0.95
Neural Network with the Levenberg-Marquardt algorithm	0.100	0.88	0.082	0.94
Neural Network with the Bayesian regularization algorithm	0.089	0.90	0.084	0.94
Neural Network with the scaled conjugate gradient algorithm	0.122	0.81	0.118	0.90

The process of developing and reconstructing the $\delta^{13}C_{DIC}$ data product is outlined in **Fig. 2**. Data collection and preprocessing were conducted following the procedures detailed in **Section 2.1** and **Section 2.2**.

The selected quality-controlled 37 cruises were used for model development, validation and test. Two of them (33RO20050111 and 33MW19930704), from the South and North Atlantic respectively, were randomly selected to form an independent test set (X1). The other 35 cruises formed dataset X2, which was further randomly split into a training set (80 %) and a validation set (20 %). The validation set was used to fine-tune hyperparameters and assess model performance, ensuring generalizability and helping identify overfitting (Wu et al., 2025). The model was trained using paired input variables: longitude (lon), latitude (lat), depth, temperature (T), salinity (S), apparent oxygen utilization (AOU), nitrate (N), silicate (Si), DIC, and atmospheric CO_2 (xCO_2), along with corresponding $\delta^{13}C_{DIC}$ values as the target variable (eq. (1)).

$$\delta^{13}C_{DIC} = f(lon, lat, depth, T, S, AOU, N, Si, DIC, xCO_2) \quad (1)$$

These input variables were selected to comprehensively capture the key physical, biological, and geochemical drivers influencing $\delta^{13}C_{DIC}$. Specifically, longitude, latitude, and depth represent the spatial location of each observation, which is essential for resolving regional and vertical patterns. T and S reflect thermohaline forcing, i.e., the physical processes such as mixing, stratification, and water mass formation that impact carbon cycling. AOU, nitrate, and silicate are indicators of biological forcing, as they are influenced by biological productivity, remineralization, and nutrient utilization. DIC is directly

related to $\delta^{13}C_{DIC}$, since $\delta^{13}C_{DIC}$ reflects the stable carbon isotopic composition of the DIC pool; thus, variations in DIC are closely tied to changes in $\delta^{13}C_{DIC}$. However, AOU, nutrients, and DIC also reflect partially physics as they are being mixed by ocean circulation. Finally, xCO_2 represents external perturbations from air-sea CO_2 exchange, which can alter both the concentration and isotopic composition of DIC. This term is necessary for predicting recent anthropogenic CO_2 influences on ocean CO_2 parameters, in particular, their decadal change rates.

The independent test set (X1), excluded entirely from training and validation, provides a final evaluation of model performance. Its role in assessing predictive skill across spatial data gaps ensures robust generalization. Finally, the trained GPR model is applied to the full set of hydrographic parameters from the GLODAPv2.2023 Atlantic dataset (https://glodap.info/index.php/merged-and-adjusted-data-product-v2-2023/) to reconstruct a basin-wide $\delta^{13}C_{DIC}$ distribution over time across the Atlantic Ocean.

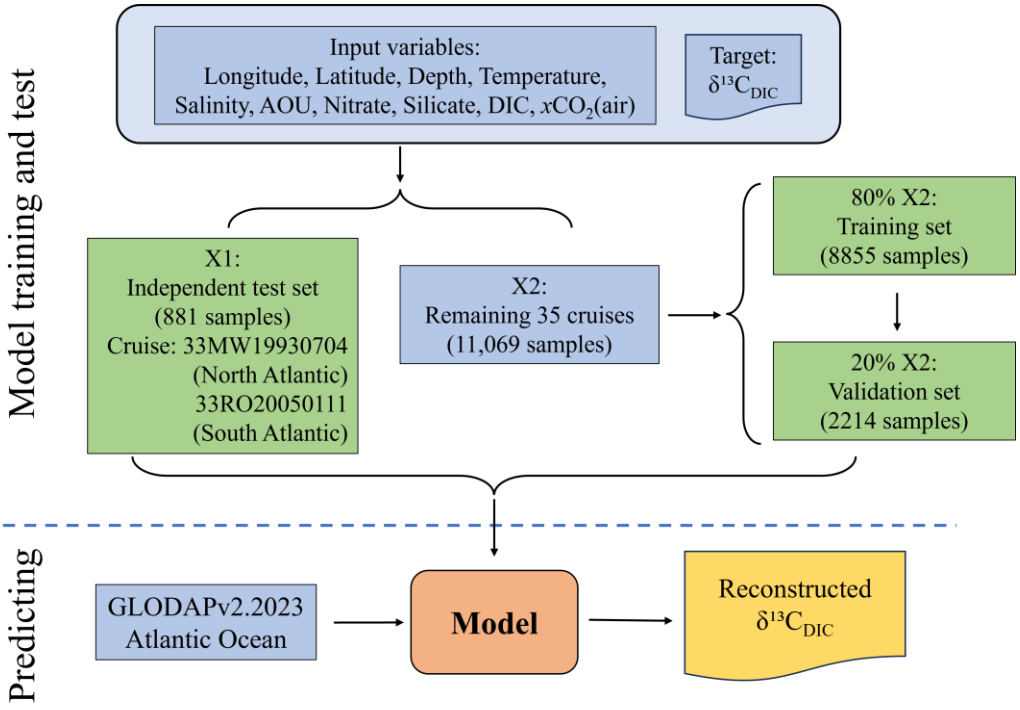

Figure 2. A flowchart illustrating the machine-learning regression model for reconstructing the $\delta^{13}C_{DIC}$ product. The blue boxes represent the input, and the yellow box represents output datasets, while the green boxes depict the model training, validation, and independent testing processes. The orange box indicates the final trained model used for prediction.

2.4 Evaluation of model

The accuracy of the model outputs was evaluated using various statistical metrics, including the R^2, RMSE, mean absolute error (MAE), and mean bias error (MBE). Among these metrics, MAE and MBE are valuable for evaluating the performance of the machine learning models. MAE quantifies the average absolute deviation between observed and predicted values; its insensitivity to outliers makes it ideal for handling the potential noise in $\delta^{13}C_{DIC}$ observational data, ensuring a robust measure of overall prediction error. MBE, by retaining the sign of deviations, identifies systematic biases (e.g., consistent overestimation or underestimation of $\delta^{13}C_{DIC}$), which is critical for refining the machine learning model.

These metrics were calculated for the training, validation, and independent test phases, as defined below:

$$R^2 = 1 - \frac{\sum_{i=1}^{N}(y_{obs,i} - y_{est,i})^2}{\sum_{i=1}^{N}(y_{obs,i} - \overline{y_{obs}})^2} \quad (2)$$

$$RMSE = \sqrt{\frac{1}{N}\sum_{i=1}^{N}(y_{obs,i} - y_{est,i})^2} \quad (3)$$

$$MAE = \frac{1}{N}\sum_{i=1}^{N}\left|y_{obs,i} - y_{est,i}\right| \quad (4)$$

$$MBE = \frac{1}{N}\sum_{i=1}^{N}\left(y_{obs,i} - y_{est,i}\right) \quad (5)$$

Here, *i* represents the *i*-th sample, $y_{obs,i}$ refers to the observed $\delta^{13}C_{DIC}$, $\overline{y_{obs}}$ is the mean of the observed $\delta^{13}C_{DIC}$ values, $y_{est,i}$ denotes the predicted $\delta^{13}C_{DIC}$ values from the final model, and N is the total number of matched samples.

2.5 Uncertainty of the reconstructed $\delta^{13}C_{DIC}$

A comprehensive assessment of uncertainty of the reconstructed $\delta^{13}C_{DIC}$ was derived via error propagation, assuming independence between distinct uncertainty sources. These sources of uncertainties include: the direct $\delta^{13}C_{DIC}$ measurement uncertainty from observations (u_{obs}), the uncertainty accumulated from the input variables (u_{inputs}), and the uncertainty induced by the mapping function (u_{map}). Following standard error propagation protocols (Hughes and Hase, 2010; Taylor, 1997), the comprehensive uncertainty of our estimated $\delta^{13}C_{DIC}$ product, $u_{\delta^{13}C_{DIC}}$, was calculated as the root sum of the squares of the individual uncertainties:

$$u_{\delta^{13}C_{DIC}} = \sqrt{u_{obs}^2 + u_{inputs}^2 + u_{map}^2} \quad (6)$$

The observational uncertainty u_{obs} inherent in $\delta^{13}C_{DIC}$ measurements varies by analytical method. For samples, when it is analyzed using IRMS, reported uncertainties range from ±0.12 ‰ (Gruber et al., 1999) to ±0.03 ‰ (Quay et al., 2003). For CRDS analysis, uncertainties are reported as ±0.07 ‰ for cruise 33RO20200321 (Gao et al., 2024) and ±0.03 ‰ for cruises 33RO20230306 and 33RO20230413 (Sun et al., 2025). Taking a conservative approach, we adopted an average u_{obs} value of 0.07 ‰.

The input variable uncertainty (u_{inputs}) accounts for uncertainties in temperature, salinity, nitrate, silicate, DIC, alkalinity, and xCO_2. Monte Carlo simulation is performed 1000 times to quantify u_{inputs}. Following Carter et al. (2024) and Wu et al. (2025), the perturbation of 0.002, 0.002, 2, 0.4, 0.4, 2 and 0.2 are randomly applied to temperature, salinity, AOU, nitrate, silicate, DIC, and xCO_2, respectively. We then recalculated $\delta^{13}C_{DIC}$ using these perturbed inputs and quantified the resulting changes. The uncertainty contribution from each variable was determined as the standard deviation of the differences between the original reconstructed $\delta^{13}C_{DIC}$ and the noise-perturbed values. The final u_{inputs} was calculated as the square root of the quadratic sum of these individual uncertainties.

$$u_{inputs}^2 = u_T^2 + u_S^2 + u_{AOU}^2 + u_N^2 + u_{Si}^2 + u_{DIC}^2 + u_{xCO_2}^2 \quad (7)$$

The uncertainty associated with the mapping function, u_{map}, is introduced within the GPR model. Here, u_{map} is primarily quantified using the GPR model's posterior predictive standard deviation (i.e., the square root of the posterior predictive variance), that is, GPR uncertainty. GPR uncertainty is a conceptually direct measure that reflects the model's inherent uncertainty in mapping environmental predictors to $\delta^{13}C_{DIC}$ across the entire prediction set. The mean value of this GPR-derived u_{map} is 0.08 ‰ across the prediction set, which captures both model variability and uncertainty related to generalization to unobserved regions. Wu et al. (2025) suggested that u_{map} may alternatively be estimated as the RMSE between reconstructed and observed $\delta^{13}C_{DIC}$ on the reconstruction dataset, and we additionally report this RMSE as a reference to facilitate compatibility. Notably, the two metrics are quantitatively similar, ensuring our core uncertainty estimate remains consistent with widely adopted reporting practices while prioritizing the GPR-derived measure's scientific rigor.

3 Results and Discussion

3.1 Evaluation of the GPR model performance

The trained GPR model exhibited robust performance and high accuracy in representing $\delta^{13}C_{DIC}$ characteristics across the Atlantic Ocean (**Fig. 3**). During the training phase, we leveraged a 10-fold cross-validation approach, selected as it is a standard pre-implemented option in MATLAB's Machine Learning Toolbox. This approach balances computational efficiency and robustness, reducing overfitting by iteratively splitting training data into 10 folds: 9 for training and 1 for validation per

iteration, with results averaged across iterations to ensure stable performance. ~~To further verify the model's robustness across different cruise combinations, we additionally conducted a cruise-separated 5-fold cross-validation as a supplementary assessment. This supplementary cross-validation yielded stable performance across all folds: per-fold RMSE ranged from 0.097‰ to 0.156‰ with an average of 0.124‰ (±0.027‰, standard deviation), and per-fold adjusted R^2 ranged from 0.74 to 0.92 with an average of 0.80 (±0.08, standard deviation). The small standard deviations of these metrics indicate that the model's performance is not sensitive to the specific combination of training cruises, confirming no significant overfitting caused by uneven sample sizes across cruises and further reinforcing the reliability of the training results.~~ Finally, the model with 10-fold cross-validation achieved an R^2 of 0.92, an RMSE of 0.083 ‰, an MAE of 0.056 ‰, and an MBE of −0.0003 ‰ during training phase (**Fig. 3a**). ~~Notably, p~~Performance metrics during the validation phase (**Fig. 3b**) were comparable to those in the training phase, demonstrating the model's strong generalization ability, i.e., its capacity to accurately predict data not used for training, and confirming its resistance to overfitting. Additionally, in the independent testing phase, the model also maintained high accuracy (R^2 = 0.95, RMSE = 0.082 ‰, MAE = 0.056 ‰, MBE = 0.007 ‰, **Fig. 3c**), with most samples clustered closely around the 1:1 line. These results indicate that the model can reliably predict $\delta^{13}C_{DIC}$ across diverse, unobserved spatial and temporal scales.

To further verify the model's robustness across different cruise combinations, we additionally conducted a cruise-separated 5-fold cross-validation. This supplementary cross-validation also yielded stable performance across all folds: per-fold RMSE ranged from 0.097‰ to 0.156‰ with an average of 0.124‰ (±0.027‰, standard deviation), and per-fold adjusted R^2 ranged from 0.74 to 0.92 with an average of 0.80 (±0.08, standard deviation). The small standard deviations of these metrics indicate that the model's performance is not sensitive to the specific combination of training cruises, confirming no significant overfitting caused by uneven sample sizes across cruises and further reinforcing the reliability of the training results. Collectively, these findings, including stable performance in 10-fold cross-validation, reliable results from the ~~supplementary~~ cruise-separated 5-fold cross-validation, consistent accuracy in the validation phase, and high reliability in independent testing, demonstrate that the GPR-based $\delta^{13}C_{DIC}$ reconstruction method is highly generalizable and robust, enabling it to accurately capture the characteristics in $\delta^{13}C_{DIC}$ and provide reliable predictions across the Atlantic Ocean.

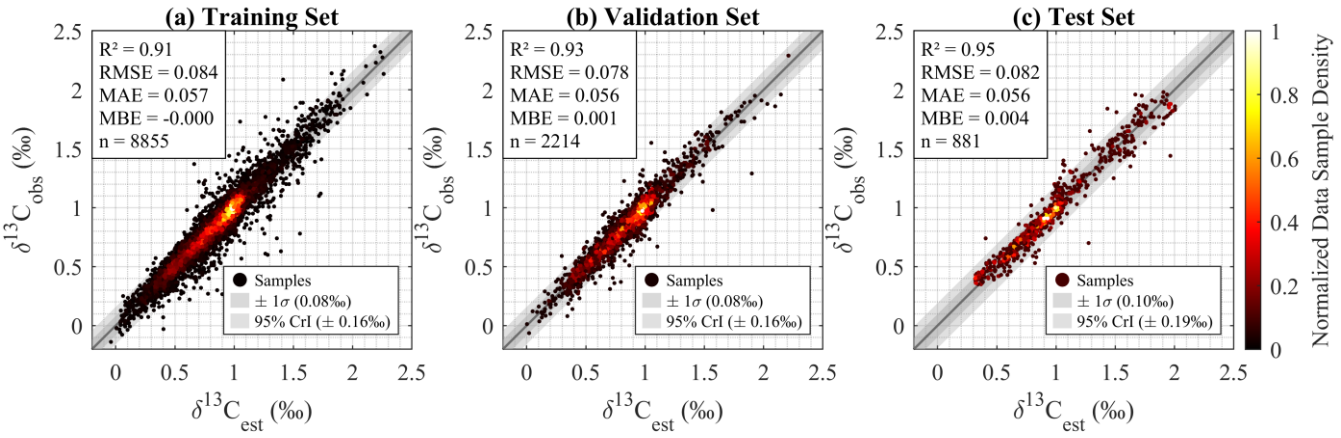

Figure 3. Regression model evaluation for $\delta^{13}C_{DIC}$ reconstruction: Density scatter plots comparing model-estimated ($\delta^{13}C_{est}$) versus observed ($\delta^{13}C_{obs}$) $\delta^{13}C_{DIC}$ values during (a) training (80 % samples from 35 cruises, with 10-fold cross-validation), (b) validation (20 % samples from 35 cruises), and (c) independent testing (samples from cruises 33RO20050111 and 33MW19930704). Statistical metrics include coefficient of determination (R^2), root-mean-square error (RMSE), mean absolute error (MAE), mean bias error (MBE), and sample size (n). Color indicates normalized local data point density within 2D bins: the plot area is divided into a 100×100 grid, raw density is the number of points per bin, and values are normalized to 0~1 (0 = sparsest, 1 = densest). Shaded bands represent predictive uncertainty, with the darker grey band showing one standard deviation (±1σ) and the lighter grey band showing the 95 % credible interval (CrI).

3.2 Evaluation of the spatial distribution of $\delta^{13}C_{DIC}$

To assess the product's ability to capture $\delta^{13}C_{DIC}$ spatial patterns and quantify biases, we utilized the $\delta^{13}C_{DIC}$ distribution from independent test cruises 33MW19930704 and 33RO20050111 (**Fig. 4**). Both cruises are part of the repeated observation A16, specifically A16N (1993) and A16S (2005), which traverses the entire Atlantic Ocean from the sub-Arctic to the Southern Ocean (**Fig. 4a**). This transect has been frequently used in existing research and textbooks to represent Atlantic-scale distributions of carbonate chemistry and other characteristics (i.e., Wanninkhof et al., 2010; Eide et al., 2017; Millero 2013), thus it is selected for evaluating the product's regional applicability.

The spatial patterns of model-estimated isotope values ($\delta^{13}C_{est}$) along cruises 33MW19930704 and 33RO20050111 effectively captured the distributional characteristics of the observed values ($\delta^{13}C_{obs}$) (**Fig. 4b vs. 4c**). The reconstructed $\delta^{13}C_{DIC}$ product exhibited a very low transect-mean bias of −0.007 ‰ with a standard deviation of 0.082 ‰ (**Fig. 4d**), highlighting the product's reliability in estimating the spatial distribution of $\delta^{13}C_{DIC}$. Spatially, the discrepancies are very small in most regions of the transect, but relatively larger in subpolar regions (around 50° S or 50° N) and vertically in the upper 500 m and below 3000 m (**Fig. 4d**).

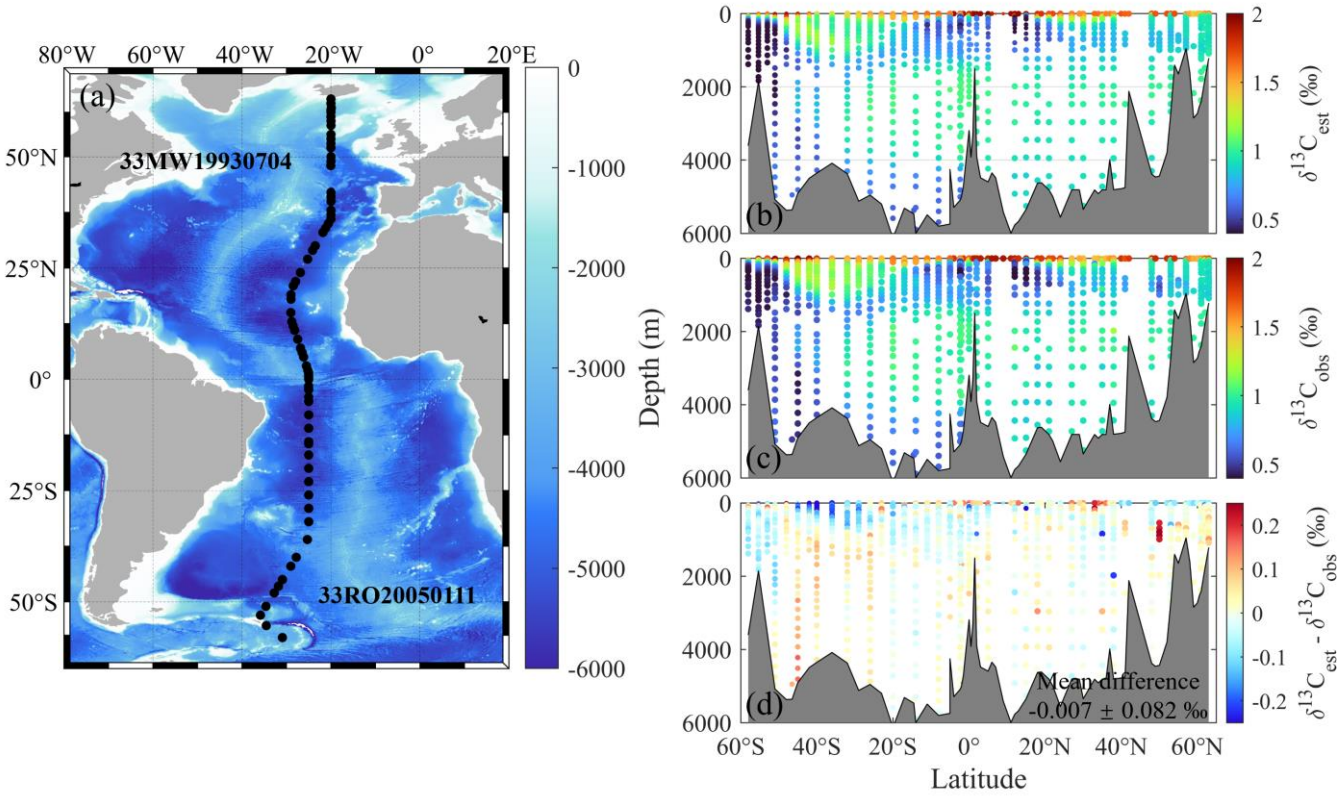

Figure 4. (a) Station locations of the independent test cruises 33MW19930704 and 33RO20050111; Depth profile of (b) model-estimated ($\delta^{13}C_{est}$) and (c) in-situ observed ($\delta^{13}C_{obs}$) $\delta^{13}C_{DIC}$ along cruises 33MW19930704 and 33RO20050111, and (d) spatial distribution of mean bias error (MBE) between $\delta^{13}C_{est}$ and $\delta^{13}C_{obs}$ for the two cruises. Positive MBE values (red) denote product overestimation, while negative values (blue) indicate underestimation relative to observation. The overall mean difference is −0.007 ± 0.082 ‰.

3.3 Evaluation of the product's uncertainty

The uncertainty of the reconstructed $\delta^{13}C_{DIC}$ product was estimated by propagating uncertainties from three primary sources: measurement (u_{obs}), input variables (u_{inputs}) and mapping (u_{map}). Detailed calculations are described in **Section 2.5** of the Methods. To ensure a conservative estimate, we adopted a uniform u_{obs} of 0.07 ‰ for all data points. u_{map} is primarily quantified using the GPR model's posterior predictive standard deviation (i.e., the square root of the posterior predictive variance), which reflects the model's inherent uncertainty in mapping environmental predictors to $\delta^{13}C_{DIC}$ and captures both model variability and generalization-related uncertainty to unobserved regions. The mean value of this GPR-derived u_{map} is 0.08 ‰. Following previous literature (Wu et al., 2025; Roobaert et al., 2024; Sharp et al., 2022), u_{map} can alternatively be estimated as the RMSE between $\delta^{13}C_{est}$ and $\delta^{13}C_{obs}$ in the training set. We additionally report this RMSE-based metric as a reference for compatibility

with existing studies, and notably, it yields a quantitatively similar value of 0.08 ‰ to the GPR-derived u_{map}. u_{inputs} was quantified via Monte Carlo simulation, considering contributions from seven environmental variables: T, S, AOU, N, Si, DIC, xCO_2. Notably, uncertainties from input variables had a nearly negligible impact, with u_{inputs} estimated at 0.009 ‰. The u_{inputs} contribution from individual input variables was decomposed as follows: temperature (4.96×10^{-5} ‰), salinity (3.62×10^{-4} ‰), nitrate (0.004 ‰), silicate (0.002 ‰), DIC (0.005 ‰), AOU (0.004 ‰), and xCO_2 (6.52×10^{-4} ‰). Overall, the reconstructed $\delta^{13}C_{DIC}$ product exhibits an average uncertainty of 0.11 ‰ for the entire Atlantic Ocean. This uncertainty is considered reasonable given the conservative estimation approach, highlighting the product's reliability for $\delta^{13}C_{DIC}$ characterization.

3.4 Additional validation using data extracted from a numerical model environment

To address the inherent limitation of observational $\delta^{13}C_{DIC}$ data (sparse and unevenly distributed across space and time), we conducted supplementary numerical model-based validation to verify the GPR model's reliability. This validation utilized well-validated ocean carbon isotope simulation data from Claret et al. (2021), which includes global monthly outputs (1990–2002) with a 1°×1° horizontal grid and 50 depth layers.

First, ~~W~~we focused on the Northeast Atlantic (30°W–5°W, 5°S–66°N) and downsampled the data to simulate observational sparsity. Limited by computational resources, we selected data from 1991 to 1995 (60 months) for validation, with 1993 (12 months) designated as an independent test set to assess generalization. The GPR model adopted the same configuration as the observational-based reconstruction (Matern 5/2 kernel, 10-fold cross-validation for hyperparameter tuning). Validation results demonstrated exceptional performance. For raw $\delta^{13}C_{DIC}$ values, R^2 exceeded 0.99 and RMSE was less than 0.015‰ across the training set, independent test set, and additional prediction set. Additionally, anomaly-based R^2 (quantifying deviations from local climatological means) ranged from 0.67 to 0.90, confirming the model's ability to capture biogeochemically meaningful spatiotemporal variations independent of large-scale offsets. For detailed data processing, parameter settings, and full validation results, refer to Appendix A.

Second, to further enhance the credibility of the GPR model in real-world application scenarios, we supplemented an additional observation- constrained~~mimetic~~ sparse validation based on the same numerical model dataset. This validation strictly mimics the spatial locations of sparse oceanographic observations by subsampling model data exclusively at the exact locations of the 37 Atlantic cruises and GLODAP locations, while preserving cruise-specific uneven sampling patterns. The results of this supplementary validation also showed robust performance. The training set achieved an R^2 of 0.99 and an RMSE of 0.009‰, the independent test set yielded an R^2 of 0.99 and an RMSE of 0.025‰, and the reconstructed values at GLODAP locations were highly consistent with the model's native values (R^2 = 0.95, RMSE = 0.080‰) (see Appendix A for details).

The ~~aforementioned~~ grid-based downsampling validation and the supplementary observation- constrained~~mimetic~~ sparse validation complement each other, jointly verifying the GPR model's robustness in reconstructing $\delta^{13}C_{DIC}$ patterns from sparse data, whether under idealized sparse grid scenarios or real observational sparse scenarios. This dual validation framework provides a solid methodological foundation for subsequent observational-based reconstruction. ~~This model-based validation demonstrates the GPR model's robustness in reconstructing 4D $\delta^{13}C_{DIC}$ patterns from sparse data, providing a solid methodological foundation for subsequent observational-based reconstruction. For detailed data processing, parameter settings, and full validation results, refer to Appendix A.~~

3.5 Reconstruction of $\delta^{13}C_{DIC}$

Here, the trained GPR model is applied to GLODAPv2.2023 hydrographic data for $\delta^{13}C_{DIC}$ reconstruction in the Atlantic Ocean, spanning the 1980s to 2021 with a small number of 1972 data points. The GLODAPv2.2023 Atlantic dataset comprises 500,137 samples, of which 8,941 contain acceptable $\delta^{13}C_{DIC}$ observations (quality flags = 2 or 6). A total of 124,643 $\delta^{13}C_{DIC}$ values can be reconstructed based on the availability of all required predictor variables (salinity, AOU, Nitrate, Silicate, and DIC). Among these, 68,435 reconstructions are considered high quality, as all six input variables have acceptable quality flags, which is approximately 7.65 times larger than the number of $\delta^{13}C_{DIC}$ observations. The remaining 56,208 reconstructions are based on input variables with unknown or lower quality and are thus assigned a quality flag of 3 (questionable). All 124,643 reconstructions, 13.9 times larger than the observation, are provided in the Supplementary Dataset, of which the questionable $\delta^{13}C_{DIC}$ samples are provided for transparency but are not recommended for routine use without further quality assessment. The following presentations and analyses are restricted to the 68,435 acceptable samples to ensure the robustness of the results unless otherwise noted.

The observed and reconstructed datasets share an intersection of 5,997 samples that have both acceptable $\delta^{13}C_{DIC}$ observations and acceptable input variables for reconstruction. These overlapping samples are used for direct model evaluation (**Fig. 5a**). The comparison between observed and reconstructed $\delta^{13}C_{DIC}$ values yields a high correlation coefficient (R^2 = 0.89), with RMSE = 0.094 ‰, MAE = 0.067 ‰, and MBE = −0.009 ‰. The mean difference between reconstruction and observation is -0.009 ± 0.097 ‰, confirming strong overall agreement. To further verify the statistical consistency between observed and reconstructed $\delta^{13}C_{DIC}$ values, we calculated Gaussian kernel density estimation (KDE) for both datasets (**Fig. 5b**). KDE is a non-parametric method for approximating probability density functions by summing Gaussian kernel functions centered at each data point (Silverman, 1986), producing a continuous estimate that is less sensitive to arbitrary bin edges. For this analysis, KDE was applied on a uniform grid spanning the full $\delta^{13}C_{DIC}$ range, with a bandwidth of 0.1 ‰ chosen to balance smoothing and resolution. No additional jittering was applied as the data contains sufficient variability to avoid overlapping artifacts. The KDE curves of observed (n = 8,941, range from −0.37 to 2.37 ‰) and reconstructed (n = 68,435, range from −0.11 to 2.36 ‰) $\delta^{13}C_{DIC}$ are highly consistent, exhibiting nearly identical unimodal distributions, with a primary peak around 1 ‰. Both curves

decline rapidly to near zero at the extremes (below ~ 0 ‰ and above ~ 2 ‰), reflecting minimal occurrence of $\delta^{13}C_{DIC}$ values in these ranges. This close alignment confirms the reconstructed $\delta^{13}C_{DIC}$ from GPR model accurately captures the central tendency, overall shape, and range of the observed $\delta^{13}C_{DIC}$ distribution.

The reconstructed dataset, which has a much larger sample size and spatially continuous coverage, exhibits minimally higher probability density than observations for $\delta^{13}C_{DIC}$ values between approximately 0.8 ‰ and 1.1 ‰, alongside a slightly sharper peak and reduced variance. This subtle distinction is a natural consequence of model smoothing intrinsic to GPR's Gaussian kernel framework and the mitigation of sampling noise in the dense, continuous reconstruction. By weighting neighbouring data points to produce spatially consistent predictions, GPR avoids overfitting to sparse extreme values often linked to transient perturbations or observational noise, an outcome aligned with the study's objective of generating a robust, representative $\delta^{13}C_{DIC}$ distribution. Overall, the KDE analysis, based on a systematic bandwidth selection and grid evaluation, underscores the strong statistical congruence between observed and reconstructed $\delta^{13}C_{DIC}$, with the minor differences being negligible relative to the model's success in replicating the core characteristics of the observed distribution.

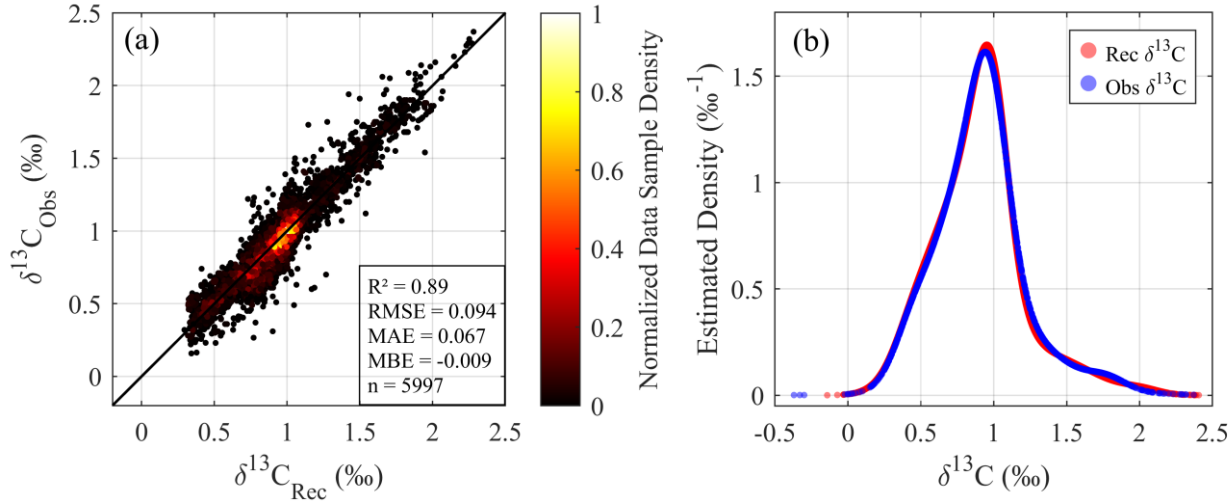

Figure 5. Comparison of observed and reconstructed $\delta^{13}C_{DIC}$ values derived from the GLODAPv2.2023 dataset. (a) Density scatter plot of observed versus reconstructed $\delta^{13}C_{DIC}$ values, using only the intersection of data points with acceptable quality available in both observed and reconstructed datasets (n = 5997). (b) Gaussian kernel density estimations (KDEs) for a comprehensive evaluation of observed and reconstructed $\delta^{13}C_{DIC}$ values. In panel b, the blue curve represents all acceptable $\delta^{13}C_{DIC}$ observations (n =8941), while the red curve indicates all acceptable reconstructed $\delta^{13}C_{DIC}$ values (n =68,435), generated by GPR model trained on the GLODAPv2.2023 dataset. The KDEs reveal the overall distribution shape, highlight differences in peak height and spread, and provide a smooth, continuous representation of probability density.

The GLODAPv2.2023 Atlantic Ocean dataset includes approximately 20,583 stations in total (**Fig. 6a**). Among these, only about 732 stations have $\delta^{13}C_{DIC}$ observations (blue points in **Fig. 6b**), collected over the four decades, reflecting the limited spatial and temporal extent of direct observations due to the high cost and complexity of $\delta^{13}C$ sampling and analysis. Using the proposed GPR model, $\delta^{13}C_{DIC}$ values have been reconstructed at roughly 4,182 stations (red points in **Fig. 6b**). This reconstructed dataset significantly expands both temporal and spatial coverage of $\delta^{13}C_{DIC}$ in the Atlantic Ocean, enabling more detailed and extensive biogeochemical analyses across the Atlantic.

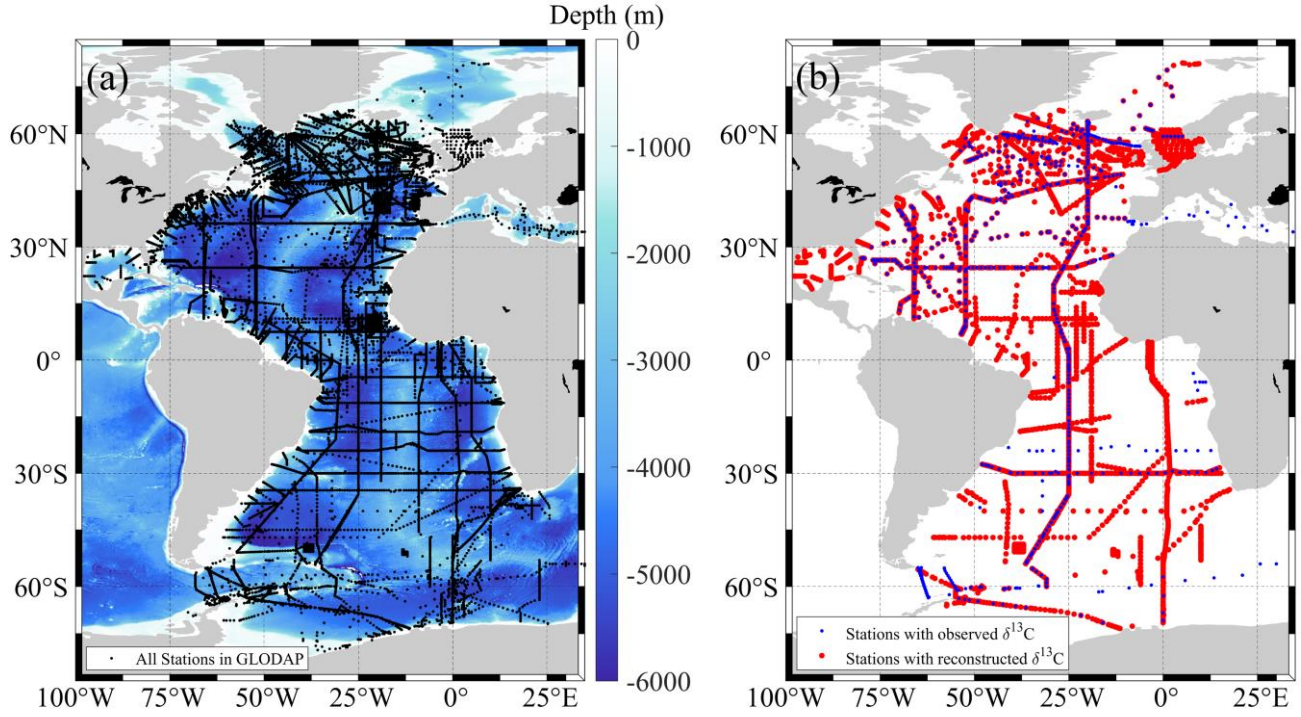

Figure 6. Station maps for the GLODAPv2.2023 Atlantic Ocean dataset. (a) Locations of all stations included in the dataset. (b) Stations with observed (blue dots) and reconstructed (red dots) $\delta^{13}C_{DIC}$.

To evaluate the spatial and temporal coverage expansion of the reconstructed $\delta^{13}C_{DIC}$ dataset, the data distributions are compared along longitude, latitude, year, and depth (**Fig. 7**). Along longitude (**Fig. 7a**), the number of reconstructed $\delta^{13}C_{DIC}$ increased several times compared to the observed, and also extended into west of 70° W and east of 0° E where there are almost no direct $\delta^{13}C_{DIC}$ observations. The latitudinal distribution (**Fig. 7b**) shows notable improvements in both hemispheres. The reconstructed dataset greatly enhanced the temporal coverage (**Fig. 7c**). There is little to no reconstructed data before 1980,

between 1984 and 1987, and in 1995. The number of reconstructed data increases significantly after the late-1980s, reaching a peak in 2003, (**Fig 7c**). Vertically, the data number of reconstructed $\delta^{13}C_{DIC}$ increased substantially throughout the water column, although numbers of both reconstructed and observed $\delta^{13}C_{DIC}$ data show exponential decrease from surface to deep water (**Fig. 7d**).

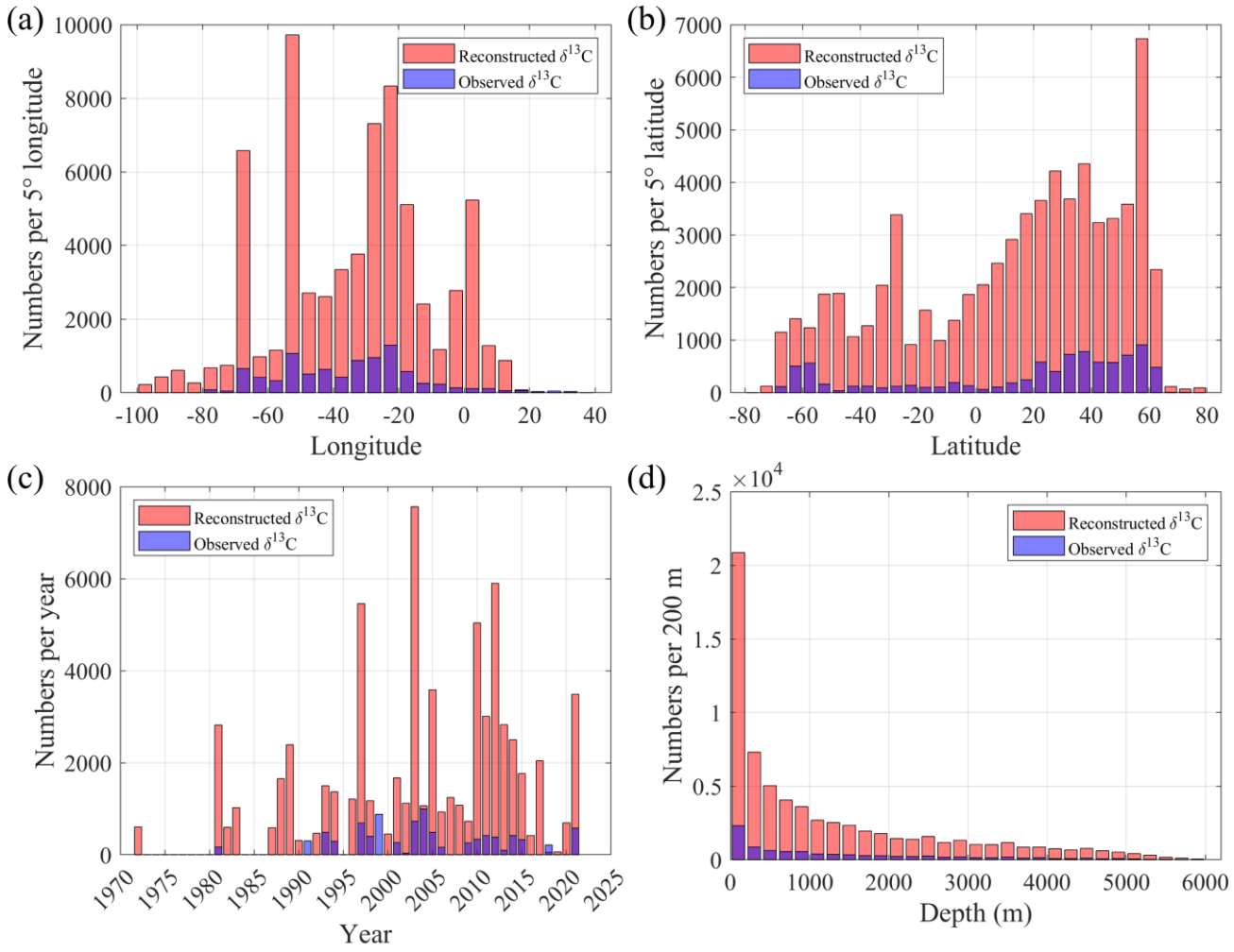

Figure 7. Comparison of the spatial, temporal, and vertical distributions of observed and reconstructed $\delta^{13}C_{DIC}$ data in the Atlantic Ocean. The number of $\delta^{13}C_{DIC}$ samples is shown by (a) longitude (per 5° bin), (b) latitude (per 5° bin), (c) year (from 1972 to 2021), and (d) depth (per 200 m interval). Red bars represent reconstructed $\delta^{13}C_{DIC}$, and blue bars indicate observed $\delta^{13}C_{DIC}$.

Overall, the reconstructed $\delta^{13}C_{DIC}$ dataset consistently demonstrated good accuracy, high correlation coefficient, low RMSE, MAE, and minimal bias across diverse environmental conditions. Spatially, the reconstruction significantly expands coverage across longitude, latitude, and depth, particularly in undersampled regions such as the South Atlantic and deeper ocean. Temporally, it enhances data availability, filling many before 1990 and after 2015, despite some limitations tied to input variable availability.

3.6 Potential Applications

The improved spatial, temporal, and vertical coverage of the reconstructed $\delta^{13}C_{DIC}$ dataset potentially contributes to the biogeochemical research and to a deeper understanding of carbon cycling processes in the Atlantic Ocean. Two specific applications are given as examples here: (1) examining the spatial patterns and decadal variability of surface $\delta^{13}C_{DIC}$ ($\leq$ 10 m), and (2) evaluating its ability to resolve vertical profiles, thereby providing insights into subsurface carbon dynamics.

To facilitate a more comprehensive understanding of the spatial and temporal dynamics of surface $\delta^{13}C_{DIC}$ in the Atlantic, **Fig. 8** illustrates how the reconstruction improves the spatial representativeness and temporal continuity of surface $\delta^{13}C_{DIC}$. The expanded spatial coverage shown in **Fig. 8a** increases the representativeness of latitudinal sample bins, reducing the influence of sparsely sampled outliers on bin means (**Fig. 8b**). For instance, observational data in the 5° – 10° S band during the 2000s show an anomalously low mean that is likely driven by a few isolated observations. In contrast, the reconstructed dataset, by supplying a larger and spatially coherent sample set, yields a mean that is more consistent with adjacent latitude bands. This effect should be understood as a reduction of sampling-driven discontinuities and noise rather than as an artificial suppression of genuine signals. Both observed and reconstructed data indicate a basin-scale decline in surface $\delta^{13}C_{DIC}$ from the 1980s to the 2010s, most pronounced in tropical and subtropical regions (approximately 35° S – 35° N), consistent with the expected Suess effect from increasing fossil-fuel CO_2 (Keeling, 1979). In contrast, the mid- to high-latitude regions exhibit more complex variability, likely reflecting the influence of regional circulation, water mass formation, and subduction processes that modulate isotopic signals on multi-decadal timescales.

To facilitate a clear and intuitive assessment of decadal distributions of observed and reconstructed surface $\delta^{13}C_{DIC}$, we employ KDE. KDE results presented in **Fig. 8c** are computed using all acceptable observed and reconstructed surface $\delta^{13}C_{DIC}$ samples within each decade and are intended to reveal the overall distributional characteristics and their evolution across decades and complement the latitude-binned means shown in **Fig. 8b**. In general, both observed and reconstructed KDE curves confirm the decadal downward shifts of $\delta^{13}C_{DIC}$ from the 1980s to the 2010s, reinforcing the notion of a basin-wide isotopic response to anthropogenic carbon inputs. And the observed and reconstructed KDE curves within each decade fall within comparable value ranges and exhibit similar peak positions, underscoring the consistency between the two datasets. Notable discrepancies arise in specific decades. For instance, in the 1980s the reconstructed KDE curve shows a dominant peak near 2 ‰ and a

secondary peak near 1.7 ‰. The latter closely corresponds to the single, broader maximum in the observational KDE curve. This discrepancy is likely attributable to the sparse observational coverage during this decade (**Fig. 8a**), which limits the representativeness of the latitudinal distribution. In the 2000s, the reconstructed KDE curve exhibits slightly greater density at the lower end of the common range (~0.5–2.0‰) than the observational KDE curve, producing a modest negative shift in central tendency while maintaining a comparable overall span. This shift is primarily attributable to a disproportionate increase in reconstructed data between 50° N and 65° N, which modifies the density structure of the distribution. These examples highlight that the reconstruction not only reproduces the principal features of the observational distributions but also mitigates the limitations imposed by sparse or uneven sampling. The reconstructed KDE curves are generally smoother and more spatially coherent than the raw observational KDE curves. The smoother and more coherent appearance of the reconstructed KDE curves reflect the underlying basin-scale $\delta^{13}C_{DIC}$ structure. This enhanced spatial consistency allows the basin-wide decadal shift toward lower $\delta^{13}C_{DIC}$ values to emerge more clearly by reducing the influence of uneven sampling. As a result, the reconstruction provides a more representative depiction of $\delta^{13}C_{DIC}$ variability across latitude and time, improving the statistical robustness and interpretability of the inferred distributional changes.

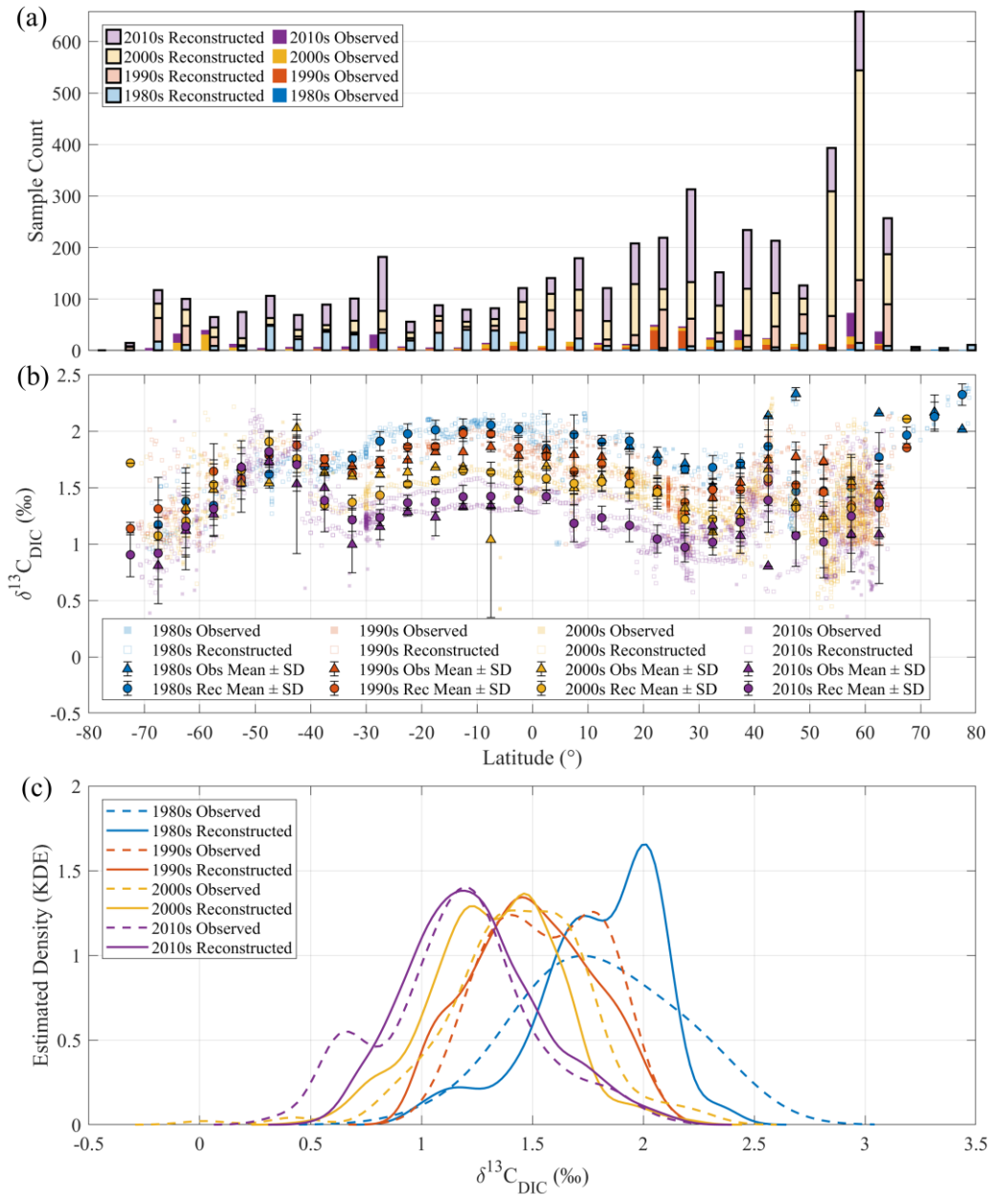

525 **Figure 8. Surface distribution of observed and reconstructed $\delta^{13}C_{DIC}$ in the Atlantic Ocean across four decades.** (a) Number of observed and reconstructed $\delta^{13}C_{DIC}$ samples within each 5° latitude band for the 1980s, 1990s, 2000s, and 2010s. For each latitude band, stacked bars represent decadal sample counts. Solid (opaque) bars indicate observations, and semi-transparent bars with black outlines indicate corresponding reconstructions. (b) Surface $\delta^{13}C_{DIC}$ distributions (depth $\leq$ 10 m) along latitude for the 1980s, 1990s, 2000s, and

2010s. Colored scatter points indicate individual $\delta^{13}C_{DIC}$ values from observations (circles) and reconstructions (dots), while the black markers with corresponding face color and error bars represent the mean ± standard deviation of $\delta^{13}C_{DIC}$ within each 5° latitude bin, triangles for observed data and diamonds for reconstructed values. (c) Gaussian kernel density estimates (KDEs) of surface $\delta^{13}C_{DIC}$ for each decade (1980s–2010s), using dashed lines for observations and solid lines for reconstructions. These KDEs reveal the decadal evolution and overall distributional characteristics of $\delta^{13}C_{DIC}$ in both datasets.

Besides horizontal distributions, the reconstructed $\delta^{13}C_{DIC}$ dataset also provides valuable insights into vertical variability. The depth profiles along the North Atlantic A16N transect in 1993, 2003, 2013, and 2023 (**Fig. 9**) show that the reconstruction substantially improves vertical resolution and continuity, especially for years with sparse measurements. For instance, the $\delta^{13}C_{DIC}$ samples were increased from 493 to 1,618 in 1993, 38 to 2,395 in 2003, and 473 to 2,787 in 2013, respectively, enhancing data coverage across depths and latitudes, facilitating the detection of temporal trends associated with ocean carbon uptake and redistribution (**Fig. 9**). The reconstructed $\delta^{13}C_{DIC}$ values for 1993, 2003, and 2013 were generated by applying the pre-trained model to input variables from the GLODAPv2.2023 Atlantic dataset. Notably, as the observational data along A16N in 2023 not included in the GLODAPv2.2023 dataset, we used the same pre-trained and validated model, relying solely on the 2023 observational input variables to produce the reconstructed values. The close alignment between 2023's reconstructed and observed data (**Fig. 9d vs. 9h**) not only reflects the model's reliability but also validates its ability to generalize, strengthening confidence in reconstructions for years with sparse measurements (e.g., 2003 with only 38 observations).

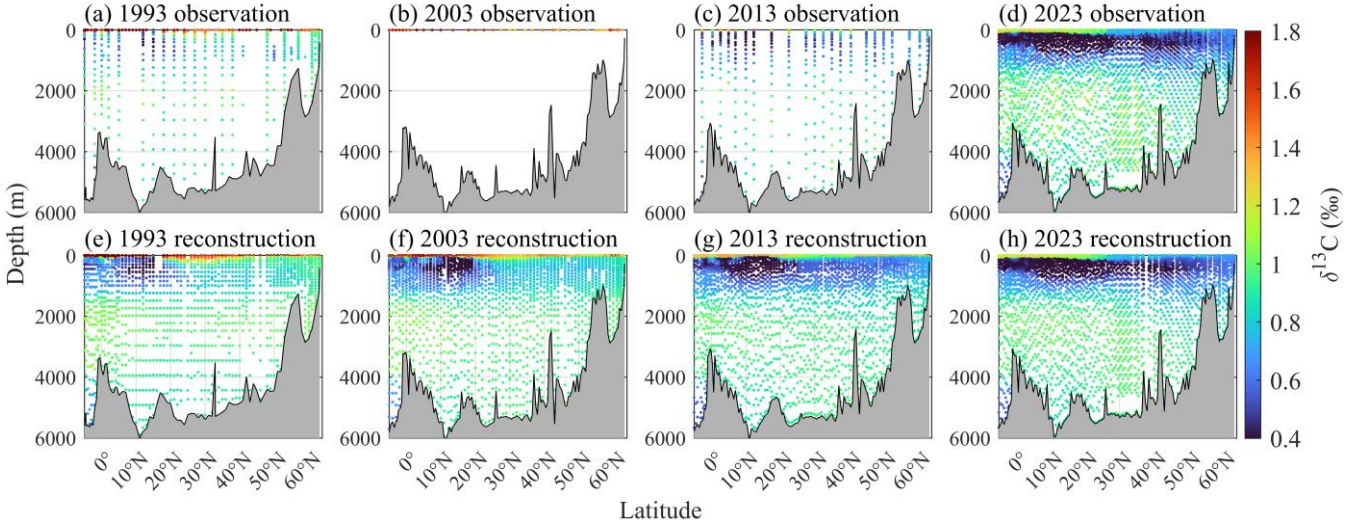

Figure 9. Enhancement of spatial resolution for $\delta^{13}C_{DIC}$ through GPR model reconstruction along North Atlantic A16N transect. Top panels (a–d) presents in-situ observed $\delta^{13}C_{DIC}$ from cruises in (a) 1993 (n = 493), (b) 2003 (surface-only, n = 38), (c) 2013 (n = 473), and (d) 2023 (n = 3,460). Bottom panels (e–h) shows corresponding reconstructed $\delta^{13}C_{DIC}$ with systematic filling of spatial gaps: (e) the

number of reconstructed $\delta^{13}C_{DIC}$ for cruise A16N in 1993 is 1,618; (f) full-depth reconstruction for cruise A16N in 2003 (n = 2,395); (g) 2013 reconstruction (n = 2,787), highlighting improved coverage compared to limited observations (n = 473); (h) the reconstruction of cruise A16N in 2023 (n=3030) validated against high-density observations. Reconstruction effectively resolves historical sampling sparsity, yielding consistent spatial resolution comparable to contemporary DIC measurements.

The enhanced vertical profiles provided by the reconstructed $\delta^{13}C_{DIC}$ dataset also enable more refined investigations into the physical and biological controls governing carbon isotope variability in the ocean interior. Joint interpretation of $\delta^{13}C_{DIC}$ with nutrients such as phosphate allows for the identification of water mass structures and biological removal and addition, shedding light on processes such as organic carbon export, remineralization, and the coupling between biological productivity and ocean circulation (e.g., Gruber et al., 1999; Eide et al., 2017). These capabilities improve the isolation of the vertical imprint of the Suess effect and facilitate the reconstruction of preindustrial $\delta^{13}C_{DIC}$, both of which are critical for assessing anthropogenic perturbations to the marine carbon cycle (Olsen et al., 2010).

$\delta^{13}C_{DIC}$ also can be used to estimate biological carbon export and net community production (NCP) (Quay et al., 2009; Yang et al., 2019). Accurate NCP estimation from $\delta^{13}C_{DIC}$ requires knowledge of both the physical supply of DIC and $\delta^{13}C_{DIC}$, typically represented by the subsurface to surface $\delta^{13}C_{DIC}$ gradient. Sparse historical $\delta^{13}C_{DIC}$ data can bias this estimate, whereas the reconstructed dataset provides a continuous field that reduces gaps and noise, enabling more reliable NCP calculations.

Importantly, the observation-constrained reconstructed $\delta^{13}C_{DIC}$ fields fill longstanding gaps in global datasets, providing a robust basis for the validation of Earth system models (e.g., Schmittner et al., 2013; Sonnerup & Quay, 2012; Claret et al., 2021). The improved coverage helps reconcile discrepancies between modeled and observed $\delta^{13}C_{DIC}$ distributions, particularly in data-sparse regions such as the deep ocean and the Southern Hemisphere. In particular, at the boundary of two water masses, the high resolution $\delta^{13}C_{DIC}$ distribution helps to validate high-resolution global physical and biogeochemical model predictions and more effectively study carbon cycle at such boundary zones.

Overall, the reconstruction effectively addresses key limitations of the observational $\delta^{13}C_{DIC}$ record, particularly data sparsity and sampling bias, providing a more continuous and spatially balanced dataset. This enables clearer identification of large-scale latitudinal gradients, decadal trends, and regional anomalies, offering a robust foundation for interpreting long-term carbon cycle dynamics.

3.7 Challenges and Limitations

Despite enhancing spatial resolution, reconstructing grid $\delta^{13}C_{DIC}$ with low uncertainty remains challenging compared to other carbonate system variables (e.g., DIC, pCO_2, TA), primarily due to limited historical observation coverage. While the dataset achieves an overall mean bias of −0.007 ‰, notable regional discrepancies persist, particularly in subpolar regions, where biases of some samples exceed 0.15 ‰. These anomalies may be attributed to highly nonlinear interactions between $\delta^{13}C_{DIC}$

and biogeochemical processes, such as upwelling-induced isotope fractionation and biological carbon pump effects (Gruber et al., 1999). Additionally, although input variables (T, S, AOU, N, Si, DIC, xCO_2) were validated to have a small impacts on reconstruction uncertainty (0.009 ‰), the exclusion of potential covariates, such as chlorophyll-a, wind speed, or nutrient gradients, may limit constraint precision.

The reconstruction approach is also subject to inherent limitations, such as spatial interpolation assumptions, uncertainty propagation, and temporal variability constraints. The GPR model assumes stationarity of $\delta^{13}C_{DIC}$ spatial covariance, a simplification that may fail in regions with abrupt bathymetric changes (e.g., the Mid-Atlantic Ridge). Such nonstationarity may introduce systematic errors in reconstructed $\delta^{13}C_{DIC}$ gradients, particularly across topographic features that influence ocean circulation and carbon transport. Cumulative uncertainties from measurement (0.07 ‰), mapping (0.08 ‰), and input variables (3.77×10^{-14} ‰) yield an overall uncertainty of 0.11 ‰, which may obscure small-scale $\delta^{13}C_{DIC}$ signals. This limitation restricts the dataset's utility for resolving fine-scale temporal trends or localized isotopic anomalies. Furthermore, the temporal sparsity of historical predictor observations restricts the resolution of interannual $\delta^{13}C_{DIC}$ variability. The application of reconstructed data to estimate the Suess effect using extended Multilinear Regression (eMLR) methods in repeated hydrographic transects requires careful consideration due to inherent uncertainties. The decadal-scale Suess effect, approximately 0.2 ‰, is often comparable to parts of discrepancy between reconstructed and observed $\delta^{13}C_{DIC}$ values. Consequently, rigorous assessment of these uncertainties is critical to ensure the reliability of decadal-scale isotopic trend estimates derived from eMLR analyses.

To address these challenges and limitations, future work will be focused on enhancing mechanistic insights into how $\delta^{13}C_{DIC}$ relates to environmental factors. Subregional partitioning strategies and variable selection methods may be developed to improve model accuracy, while process-based knowledge also should be integrated to identify optimal predictor variables and refine regionalization schemes for biogeochemical heterogeneity. Additionally, uncertainty mitigation techniques will be coupled with emerging high-resolution observations from autonomous platforms, which will be leveraged to refine spatial resolution to fixed grids. Furthermore, physics-informed reconstruction frameworks (e.g., Bennington et al., 2022) have the potential to extend $\delta^{13}C_{DIC}$ records across pre- and post-satellite eras using proxy variables for historical biological productivity, improving temporal consistency and Suess effect estimation via eMLR methods by reducing uncertainties in decadal-scale trend analyses.

4 Conclusion

This study reconstructs Atlantic Ocean $\delta^{13}C_{DIC}$ using a GPR model trained on 37 secondary quality-controlled cruises selected from 51 compiled historical datasets, including a high-resolution 2023 A16N transect. GPR was chosen for its ability to capture

nonlinear relationships, outperforming other machine-learning models in preliminary tests (lowest RMSE and highest R^2). Additionally, the method's robustness was validated using numerical model data (Claret et al., 2021), with both grid-based downsampling and observation-constrained~~mimetic~~ sparse sampling validation frameworks, confirming not only the GPR model's stability but also the high~~its~~ reliability in $\delta^{13}C_{DIC}$ reconstruction. The trained GPR model achieved an average bias of only -0.007 ± 0.082 ‰ and an overall uncertainty of 0.11 ‰, with error contributions from measurement, mapping and input-variable.

Applying GLODAPv2.2023 Atlantic dataset as predictors, the reconstruction expanded the acceptable $\delta^{13}C_{DIC}$ samples from 8,941 to 68,435, representing a substantial 7.65-fold increase compared to the original dataset. This extensive dataset significantly improves spatial coverage in longitude, latitude, and depth and enhances temporal continuity of $\delta^{13}C_{DIC}$ observations over the past four decades.

Multiple pieces of evidence attest to reliability and superiority of the reconstructed dataset. Statistical diagnostics demonstrate strong model skill in both cross-validation and independent testing stages, as well as reconstruction stage. The reconstruction preserves decadal variability at the sea surface $\delta^{13}C_{DIC}$ and in depth-profiles and agrees with high-density contemporary observations such as the 2023 A16N transect. Distributional metrics, exemplified by smoothed and stable KDE curves, suggest that the reconstruction mitigates sampling noise while retaining meaningful spatiotemporal signals.

The broad spatial coherence and high coverage of the reconstructed $\delta^{13}C_{DIC}$ enable systematic analysis of large-scale gradients, detection of regional anomalies, and investigation of tracer relationships with nutrients such as phosphate, supporting a wide range of carbon cycle studies. It also provides a valuable baseline for evaluation of Earth system models, for improving estimates of preindustrial and anthropogenic $\delta^{13}C_{DIC}$, and for extending isotopic records used in climate reanalysis.

Despite these advances, some challenges and limitations remain. Regional biases persist, likely reflecting highly nonlinear biogeochemical interactions and the GPR assumption of spatial covariance stationarity, which may break down over complex bathymetry. Small-scale features can be obscured by cumulative uncertainty propagation and temporal inconsistencies persist in certain derived quantities. Future efforts will be needed on assimilating higher-resolution observations to enhancing the mechanistic understanding of relationships between $\delta^{13}C_{DIC}$ and environment factors, developing tailored subregional modelling frameworks and exploiting advanced machine-learning techniques to capture nonstationary spatial features. These efforts will refine spatial and temporal fidelity, reduce uncertainties and gain deeper mechanistic insight into ocean carbon cycle dynamics.

5 Data availability

The quality-controlled and reconstructed $\delta^{13}C_{DIC}$ in the Atlantic Ocean are available as two NetCDF/Excel files at https://doi.org/10.5281/zenodo.18481145 ~~https://doi.org/10.5281/zenodo.16907402~~ (Gao et al., 2025).

6 Code availability

The MATLAB code used to process the data and create the figures included in this paper is provided at https://github.com/huigao109/ReC13_ML

Appendix A: Numerical Model-based Validation of the GPR Method for 4D $\delta^{13}C_{DIC}$ Reconstruction

The main text focuses on reconstructing $\delta^{13}C_{DIC}$ in the Atlantic Ocean using sparse observational data. However, validating machine learning methods solely with observations faces inherent limitations: observational data are spatially-temporally discrete, unevenly distributed, and lack an explicit reference distribution for rigorous accuracy assessment. To address this gap, we conducted supplementary numerical model-based validation using well-validated ocean carbon isotope simulation data (Claret et al., 2021). This validation aims to evaluate the GPR model's ability to reconstruct 4D (longitude-latitude-depth-time) $\delta^{13}C_{DIC}$ patterns from sparse, perturbed data and complement observational validation to strengthen the methodological rigor.

The original simulation dataset from Claret et al. (2021) features monthly outputs from 1990 to 2002, a 1° × 1° horizontal grid (global longitude-latitude) and 50 depth layers covering the full water column. Notably, the dataset does not provide nitrate (N) or silicate (Si) data but includes phosphate (PO_4) data. We conducted sensitivity tests on observational dataset to assess the impact of input variable selection, comparing two variable sets: one including longitude, latitude, depth, T, S, AOU, nitrate, silicate, DIC, and xCO_2, and the other replacing N and Si with PO_4. Results showed no significant performance differences between the two sets (the change of RMSE < 2%), confirming that PO_4 can effectively serve as a proxy for the missing nutrients.

Due to the massive size of the original dataset (exceeding computational feasibility for standard Machine Learning workflows), we processed the data as follows: 1) We focused on the Northeast Atlantic (30°W–5°W, 5°S–66°N), a region with representative $\delta^{13}C_{DIC}$ spatial gradients and relevance to the main text's Atlantic-focused reconstruction. 2) To simulate observational sparsity, we subsampled the 1° × 1° grid at 5-grid intervals, resulting in a horizontal resolution of 5° × 5° (5 longitude points × 19 latitude points within the study region). 3) For the vertical dimension, we retained depth layers within the upper 1500 m, and subsampled 1 point every 4 layers, yielding 10 vertical layers. Temporally, we selected data from 1991 to 1995 (60 months) for validation, with 1993 (12 months) designated as an independent test set to assess generalization.

Each month's theoretical sample size after downsampling is 950, and after excluding grid cells with invalid data, the monthly effective sample size is 799. Over 60 months, the total sample size is 47,940. Given this scale, we randomly selected 1/3 of the data (15,980 samples) for model training, validation, and independent testing, with the remaining 2/3 (31,960 samples) as an additional prediction set to further verify generalization to unseen 4D grid points.

The GPR model used in this validation adopted the same configuration as the main text: Matern 5/2 kernel, and hyperparameter tuning via 10-fold cross-validation within the training set. This consistency ensures the validation results are directly comparable to the main text's observational-based performance. For dataset partitioning, the training set comprised 80% of the 1/3 subsampled data covering 1991–1992 and 1994–1995 (excluding 1993), while the internal validation set included 20% of the 1/3 subsampled data from the same non-1993 years as the training set and was used for hyperparameter tuning. The independent test set included all 1993 data within the 1/3 subsampled pool to ensure temporal independence from training/validation data, and the additional prediction set consisted of the remaining 2/3 of the full downsampled data (31,960 samples) spanning 1991–1995 to verify reconstruction of dense 4D grids. Consistent with the main text, we used RMSE and R^2 to assess point prediction accuracy. We further introduced anomaly-based R^2 ($R^2_{anomaly}$), which is calculated from anomalies relative to the local mean or climatology, where the local climatological mean denotes the 5-year monthly average of $\delta^{13}C_{DIC}$ at each longitude-latitude-depth grid, to quantify the model's ability to capture biogeochemically meaningful deviations from large-scale background trends. By isolating these deviations from the climatological baseline, this approach reduces the influence of large-scale offsets and thereby provides a more realistic assessment of the model's capacity to reproduce spatial–temporal variations.

The GPR model achieved exceptional performance in the model-based validation, confirming its robustness for 4D $\delta^{13}C_{DIC}$ reconstruction. For raw $\delta^{13}C_{DIC}$ values (total signal), the internal validation set yielded $R^2 > 0.99$ and RMSE = 0.006‰, while the independent test set showed $R^2 > 0.99$ and RMSE = 0.012‰ (Figure A1), and the additional prediction set exhibited $R^2 > 0.99$ and RMSE = 0.013‰ (Figure A2). Critically, the anomaly-based R^2 values further demonstrated the model's capacity to capture ecologically relevant variability: the training set reached an $R^2_{anomaly}$ of 0.90, the temporally independent test set achieved an $R^2_{anomaly}$ of 0.67, and the additional prediction set (unseen 4D grid points) showed an $R^2_{anomaly}$ of 0.84. These results indicate the model nearly perfectly reproduces the absolute $\delta^{13}C_{DIC}$ values from the Claret model, while also effectively reconstructing biogeochemically meaningful anomalies such as seasonal cycling and regional biogeochemical deviations independent of large-scale climatological offsets. The consistent anomaly-based performance across the temporally unseen independent test set and the spatiotemporally dense, unseen additional prediction set confirms robust generalization to unobserved 4D $\delta^{13}C_{DIC}$ patterns. The slightly lower $R^2_{anomaly}$ of 0.67 for the independent test set may stem from the limited sample size. Using only 1/3 of the data rather than the full dataset likely insufficiently captures the unique spatiotemporal variability of 1993. Notably, the higher $R^2_{anomaly}$ of the additional prediction set implies that a larger sample size may better

reflect the spatiotemporal characteristics of $\delta^{13}C_{DIC}$. However, in this paper, our focus is on large scale features over long timescales. We will examine this issue in future studies.

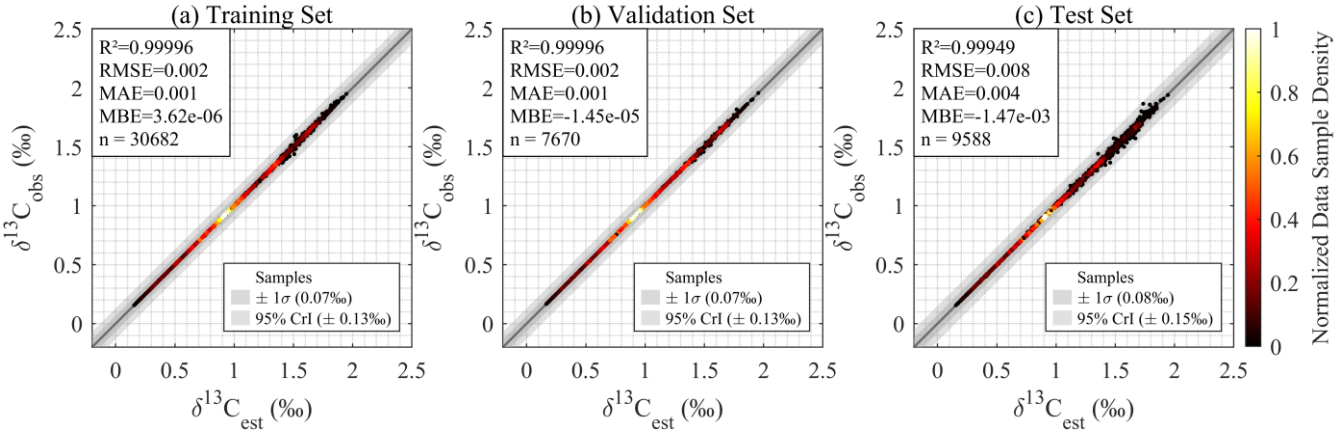

Figure A1. GPR model evaluation for numerical model $\delta^{13}C_{DIC}$ reconstruction: Density scatter plots comparing GPR model-estimated ($\delta^{13}C_{est}$) versus numerical model outputs $\delta^{13}C_{DIC}$ ($\delta^{13}C_{obs}$) values during (a) training, (b) validation, and (c) independent testing.

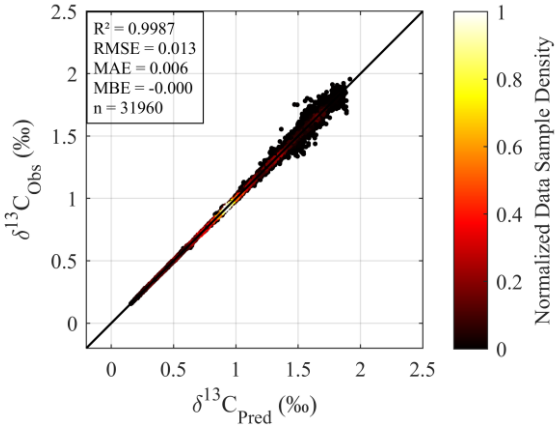

Figure A2 Density scatter plot comparing numerical model outputs $\delta^{13}C_{DIC}$ ($\delta^{13}C_{Obs}$) versus predicted $\delta^{13}C_{DIC}$ ($\delta^{13}C_{Pred}$) values.

This model-based validation complements the observational validation by addressing two critical limitations of sparse, uneven coverage data. The exceptional performance ($R^2 > 0.99$, RMSE < 0.015‰) confirms that the GPR model can accurately reconstruct 4D $\delta^{13}C_{DIC}$ patterns, validating its performance. In the meantime, meaningful anomaly-based R^2 values ranging from 0.67 to 0.90 validate the model's capacity to capture ecologically and biogeochemically relevant variations beyond simply reproducing large-scale background trends. This validation strengthens confidence that the reconstructed dataset is not

constrained by methodological flaws. Instead, its limitations stem from inherent observational uncertainties such as sparse sampling and unmodeled biogeochemical variability, ensuring the dataset reliably captures the spatial-temporal dynamics of $\delta^{13}C_{DIC}$ in the Atlantic Ocean.

To further enhance the credibility of the GPR model and the reconstructed dataset, and to address the concern that idealized grid-based subsampling may not fully reflect real-world observational scenarios, we supplemented an additional model-based validation that strictly mimics the spatial-temporal characteristics of sparse oceanographic observations. This validation focuses on evaluating the model's ability to learn from observation-like sparse data and generalize to target locations (e.g., GLODAP sampling locations), which is directly aligned with the core application scenario of the main text's $\delta^{13}C_{DIC}$ reconstruction work.

The validation design strictly follows the real observational framework: 1) We subsampled the Claret et al. (2021) model data exclusively at the exact spatial locations of the 37 Atlantic cruises used in the main text's training, validation, and test sets, as well as the GLODAP sampling locations employed for prediction. Given that the model data only spans 1990–2002, we mapped observational data from other decades (e.g., 2000–2009 observations to 1990–1999 model data) to maintain a sample size comparable to the full observational dataset. This design exactly replicates the sparse, heterogeneous distribution of real oceanographic observations, eliminating the idealized grid-based subsampling bias. 2) The GPR model adopted the same parameter settings as the aforementioned grid-based validation, ensuring consistency and comparability of results across different validation scenarios. 3) Consistent with the previous validation, we used R^2, RMSE, MAE and MBE to assess the accuracy of point predictions.

The results of this observation-constrained~~mimetic~~ sparse validation demonstrate robust performance of the GPR model (Figure A3). The training set achieves an R^2 of 0.999 and an RMSE of 0.009‰, the validation set shows an R^2 of 0.9985 and an RMSE of 0.012‰, and the independent test set yields an R^2 of 0.9950 and an RMSE of 0.025‰. These metrics confirm that the model can learn robustly from sparse, observation-like data and generalize effectively to unseen cruises, which is consistent with the performance of the grid-based validation and further verifies the model's stability.

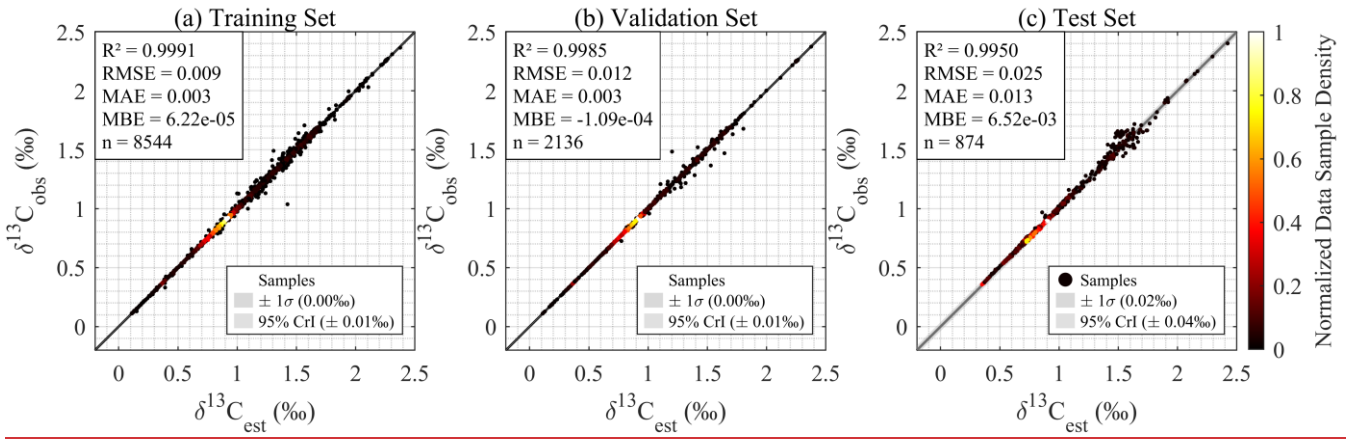

Figure A3. GPR model evaluation for numerical model $\delta^{13}C_{DIC}$ reconstruction (observation-constrained~~mimetic~~ sparse sampling): Density scatter plots comparing GPR model-estimated ($\delta^{13}C_{est}$) versus numerical model outputs $\delta^{13}C_{DIC}$ ($\delta^{13}C_{obs}$) values during (a) training, (b) validation, and (c) independent testing.

For the prediction phase at GLODAP locations (Figure A4), the reconstructed $\delta^{13}C_{DIC}$ values align closely with the model's native values, with an R^2 of 0.95 and an RMSE of 0.080‰. High-density data points cluster tightly along the 1:1 line (Figure A4a), indicating excellent consistency between the reconstructed results and the true model values. Some minor deviations from the 1:1 line are likely attributed to inherent uncertainties and biases in the numerical model itself, rather than the GPR model's performance. The KDE analysis (Figure A4b) further underscores the strong statistical congruence between the numerical model δ13C values and the reconstructed estimates, with minor differences being negligible relative to the model's success in replicating the core characteristics of the native distribution.

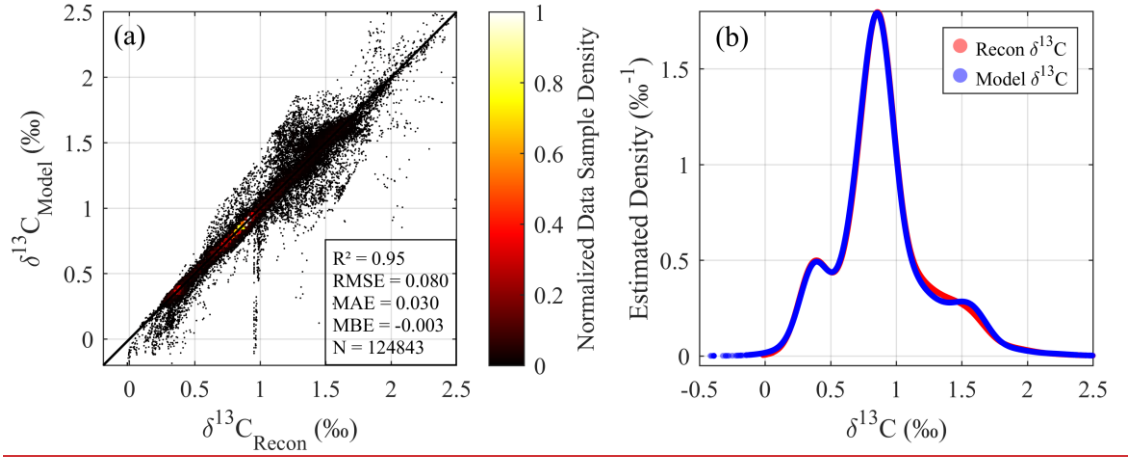

Figure A4. Comparison of model and reconstructed δ13C values at GLODAP locations (observation-constrained~~mimetic~~ sparse sampling): (a) Density scatter plot of model versus reconstructed δ13C values (n = 124,843). (b) Gaussian kernel density estimations (KDEs) for a comprehensive evaluation of model and reconstructed δ13CDIC values.

This supplementary observation-constrained~~mimetic~~ validation complements the previous grid-based validation, jointly reinforcing the reliability of the GPR model and the reconstructed data from two dimensions: "idealized grid sparse scenario" and "real observational sparse scenario". The consistent excellent performance across both validation frameworks confirms that the GPR model can not only accurately reconstruct $\delta^{13}C_{DIC}$ patterns from sparse grid data but also reliably learn from real-world sparse observational data and generalize to target application locations. This dual validation provides solid methodological support for the rigor of the main text's $\delta^{13}C_{DIC}$ reconstruction work, further confirming that the reconstructed dataset can effectively address the limitations of sparse observational data and meet the needs of Atlantic carbon cycle research.

Author contribution

H. G.: Conceptualization, data curation, formal analysis, methodology, software, visualization, writing – original draft preparation, writing – review & editing. **Z. W.**: Validation, methodology, writing – review & editing. **Z. S.**: Validation, writing – review & editing. **D. C.**: Validation, methodology, writing – review & editing. **M. J.**: Conceptualization, validation, writing – review & editing. **W-J. C.**: Conceptualization, funding acquisition, writing – review & editing, project administration, supervision.

Competing interests

The authors declare that they have no conflict of interest.

Disclaimer

Special issue statement

Acknowledgments

The authors gratefully acknowledge all researchers, principal investigators, captains, and crew members who contributed their time at sea and in the laboratory to collect, analyze, and curate the datasets used in this study. We thank the providers and

maintainers of the GLODAP, OCADS, and CCHDO databases, as well as the creators of the internally consistent $\delta^{13}C_{DIC}$ dataset for the North Atlantic Ocean (NAC13v1; Becker et al., 2016), for making their data openly available. The authors used ChatGPT for grammar and language polishing; all scientific content, interpretations, and conclusions are the sole responsibility of the authors.

Financial support

This research is supported by the US National Science Foundation awards (OCE-2123768 & OCE-25A00158) to W-J.C.

References

Alling, V., Porcelli, D., Mörth, C.-M., Anderson, L. G., Sanchez-Garcia, L., Gustafsson, Ö., Andersson, P. S., and Humborg, C.: Degradation of terrestrial organic carbon, primary production and out-gassing of CO_2 in the Laptev and East Siberian Seas as inferred from $\delta^{13}C$ values of DIC, Geochimica et Cosmochimica Acta, 95, 143–159, https://doi.org/10.1016/j.gca.2012.07.028, 2012.

Becker, M., Andersen, N., Erlenkeuser, H., Humphreys, M. P., Tanhua, T., and Körtzinger, A.: An internally consistent dataset of δ13C-DIC in the North Atlantic Ocean – NAC13v1, Earth System Science Data 8: 559-570, https://doi.org/10.5194/essd-8-559-2016, 2016.

Bennington, V., Galjanic, T., and McKinley, G. A.: Explicit Physical Knowledge in Machine Learning for Ocean Carbon Flux Reconstruction: The pCO_2 -Residual Method, J Adv Model Earth Syst, 14, e2021MS002960, https://doi.org/10.1029/2021MS002960, 2022.

Carter, B. R., Sharp, J. D., Dickson, A. G., Álvarez, M., Fong, M. B., García-Ibáñez, M. I., Woosley, R. J., Takeshita, Y., Barbero, L., Byrne, R. H., Cai, W., Chierici, M., Clegg, S. L., Easley, R. A., Fassbender, A. J., Fleger, K. L., Li, X., Martín-Mayor, M., Schockman, K. M., and Wang, Z. A.: Uncertainty sources for measurable ocean carbonate chemistry variables, Limnology & Oceanography, 69, 1–21, https://doi.org/10.1002/lno.12477, 2024.

Claret, M., Sonnerup, R. E., and Quay, P. D.: A Next Generation Ocean Carbon Isotope Model for Climate Studies I: Steady State Controls on Ocean 13 C, Global Biogeochemical Cycles, 35, e2020GB006757, https://doi.org/10.1029/2020GB006757, 2021.

Deng, X., Li, Q., Su, J., Liu, C.-Y., Atekwana, E., and Cai, W.-J.: Performance evaluations and applications of a δ13C-DIC analyzer in seawater and estuarine waters, Science of The Total Environment, 833, 155013, https://doi.org/10.1016/j.scitotenv.2022.155013, 2022.

Eide, M., Olsen, A., Ninnemann, U. S., and Johannessen, T.: A global ocean climatology of preindustrial and modern ocean δ 13 C, Global Biogeochemical Cycles, 31, 515–534, https://doi.org/10.1002/2016GB005473, 2017.

Esposito, M., Achterberg, E. P., Bach, L. T., Connelly, D. P., Riebesell, U., and Taucher, J.: Application of Stable Carbon Isotopes in a Subtropical North Atlantic MesocosmStudy: A New Approach to Assess CO2 Effects on the Marine Carbon Cycle, Front. Mar. Sci., 6, 616, https://doi.org/10.3389/fmars.2019.00616, 2019.

Gao, H., Cai, W., Jin, M., Dong, C., and Timmerman, A. H. V.: Ocean Ventilation Controls the Contrasting Anthropogenic CO_2 Uptake Rates Between the Western and Eastern South Atlantic Ocean Basins, Global Biogeochemical Cycles, 36, e2021GB007265, https://doi.org/10.1029/2021GB007265, 2022.

Gao, H., Jin, M., Zhao, H., Hussain, N., and Cai, W.: Using DIC-δ13 C Pair to Constrain Anthropogenic Carbon Increase in the Southeastern Atlantic Ocean Over the Most Recent Decade (2010–2020), JGR Oceans, 129, e2024JC021586, https://doi.org/10.1029/2024JC021586, 2024.

Gao, H., Wu, Z., Sun, Z., Cai, D., Jin, M., & Cai, W.-J.: Reconstruction of δ^{13}CDIC in the Atlantic Ocean [Data set]. Zenodo. https://doi.org/10.5281/zenodo.16907402, 2025.

Gregor, L. & Gruber, N. OceanSODA-ETHZ: a global gridded data set of the surface ocean carbonate system for seasonal to decadal studies of ocean acidification. Earth System Science Data 13, 777-808. https://doi.org/10.5194/essd-13-777-2021, 2021.

Gruber, N., Keeling, C. D., Bacastow, R. B., Guenther, P. R., Lueker, T. J., Wahlen, M., Meijer, H. A. J., Mook, W. G., and Stocker, T. F.: Spatiotemporal patterns of carbon-13 in the global surface oceans and the oceanic suess effect, Global Biogeochem. Cycles, 13, 307–335, https://doi.org/10.1029/1999GB900019, 1999.

Hughes, I. and Hase, T. P. A.: Measurements and their uncertainties: a practical guide to modern error analysis, New York : Oxford University Press, Oxford, 136 pp., 2010.

Keeling, C. D.: The Suess effect: 13Carbon-14Carbon interrelations, Environment International, 2, 229–300, https://doi.org/10.1016/0160-4120(79)90005-9, 1979.

Körtzinger, A., Quay, P. D., and Sonnerup, R. E.: Relationship between anthropogenic CO 2 and the 13 C Suess effect in the North Atlantic Ocean, Global Biogeochemical Cycles, 17, https://doi.org/10.1029/2001GB001427, 2003.

Kroopnick, P.: The distribution of 13C in the Atlantic Ocean, Earth and Planetary Science Letters, 49(2): 469-484, https://doi.org/10.1016/0012-821X(80)90088-6, 1980.

Kroopnick, P.: The distribution of 13C of ΣCO2 in the world oceans, Deep Sea Research Part A. Oceanographic Research Papers, 32(1): 57-84, https://doi.org/10.1016/0198-0149(85)90017-2, 1985.

Kroopnick, P.: Isotopic fractionations during oxygen consumption and carbonate dissolution within the North Atlantic Deep Water, Earth and Planetary Science Letters, 49, 485–498, https://doi.org/10.1016/0012-821X(80)90089-8, 1980.

Kwon, E. Y., DeVries, T., Galbraith, E. D., Hwang, J., Kim, G., and Timmermann, A.: Stable Carbon Isotopes Suggest Large Terrestrial Carbon Inputs to the Global Ocean, Global Biogeochemical Cycles, 35, e2020GB006684, https://doi.org/10.1029/2020GB006684, 2021.

Landschützer, P., Gruber, N. & Bakker, D. C. E. Decadal variations and trends of the global ocean carbon sink. Global Biogeochemical Cycles 30, 1396-1417. https://doi.org/10.1002/2015gb005359, 2016.

Lauvset, S. K. and Tanhua, T.: A toolbox for secondary quality control on ocean chemistry and hydrographic data, Limnol. Oceanogr. Methods, 13, 601–608, https://doi.org/10.1002/lom3.10050, 2015.

Lauvset, S. K., Lange, N., Tanhua, T., Bittig, H. C., Olsen, A., Kozyr, A., Álvarez, M., Azetsu-Scott, K., Brown, P. J., Carter, B. R., Cotrim Da Cunha, L., Hoppema, M., Humphreys, M. P., Ishii, M., Jeansson, E., Murata, A., Müller, J. D., Pérez, F. F., Schirnick, C., Steinfeldt, R., Suzuki, T., Ulfsbo, A., Velo, A., Woosley, R. J., and Key, R. M.: The annual update GLODAPv2.2023: the global interior ocean biogeochemical data product, Earth Syst. Sci. Data, 16, 2047–2072, https://doi.org/10.5194/essd-16-2047-2024, 2024.

Lima, I. D., Wang, Z. A., Cameron, L. P., Grabowski, J. H., & Rheuban, J. E.: Predicting Carbonate Chemistry on the Northwest Atlantic Shelf Using Neural Networks. Journal of Geophysical Research: Biogeosciences, 128(7), e2023JG007536, https://doi.org/10.1029/2023JG007536, 2023.

Liu, B., Six, K. D., and Ilyina, T.: Incorporating the stable carbon isotope13 C in the ocean biogeochemical component of the Max Planck Institute Earth System Model, Biogeosciences, 18, 4389–4429, https://doi.org/10.5194/bg-18-4389-2021, 2021.

Millero, F. J.: Chemical oceanography, Vol. 30. CRC press, 2005.

Olsen, A., Key, R. M., Van Heuven, S., Lauvset, S. K., Velo, A., Lin, X., Schirnick, C., Kozyr, A., Tanhua, T., Hoppema, M., Jutterström, S., Steinfeldt, R., Jeansson, E., Ishii, M., Pérez, F. F., and Suzuki, T.: The Global Ocean Data Analysis Project version 2 (GLODAPv2) – an internallyconsistent data product for the world ocean, Earth Syst. Sci. Data, 8, 297–323, https://doi.org/10.5194/essd-8-297-2016, 2016.

Olsen, A. and Ninnemann, U.: Large δ 13 C Gradients in the Preindustrial North Atlantic Revealed, Science, 330, 658–659, https://doi.org/10.1126/science.1193769, 2010.

Quay, P. D., Tilbrook, B., and Wong, C. S.: Oceanic Uptake of Fossil Fuel CO2 : Carbon-13 Evidence, Science, 256, 74–79, https://doi.org/10.1126/science.256.5053.74, 1992.

Quay, P., Sonnerup, R., Westby, T., Stutsman, J., and McNichol, A.: Changes in the 13 C/ 12 C of dissolved inorganic carbon in the ocean as a tracer of anthropogenic CO 2 uptake, Global Biogeochemical Cycles, 17, https://doi.org/10.1029/2001GB001817, 2003.

Quay, P., Sonnerup, R., Stutsman, J., Maurer, J., Körtzinger, A., Padin, X. A., and Robinson, C.: Anthropogenic CO 2 accumulation rates in the North Atlantic Ocean from changes in the 13 C/ 12 C of dissolved inorganic carbon, Global Biogeochemical Cycles, 21, 2006GB002761, https://doi.org/10.1029/2006GB002761, 2007.

Quay, P. D., Stutsman, J., Feely, R. A., and Juranek, L. W.: Net community production rates across the subtropical and equatorial Pacific Ocean estimated from air-sea δ 13 C disequilibrium, Global Biogeochemical Cycles, 23, 2008GB003193, https://doi.org/10.1029/2008GB003193, 2009.

Quay, P., Sonnerup, R., Munro, D., and Sweeney, C.: Anthropogenic CO2 accumulation and uptake rates in the Pacific Ocean based on changes in the 13 C/ 12 C of dissolved inorganic carbon, Global Biogeochem. Cycles, 31, 59–80, https://doi.org/10.1002/2016GB005460, 2017.

Quay, P., Emerson, S., and Palevsky, H.: Regional Pattern of the Ocean's Biological Pump Based on Geochemical Observations, Geophysical Research Letters, 47, e2020GL088098, https://doi.org/10.1029/2020GL088098, 2020.

Quay, P.: Organic Matter Export Rates and the Pathways of Nutrient Supply in the Ocean, Global Biogeochemical Cycles, 37, e2023GB007855, https://doi.org/10.1029/2023GB007855, 2023.

Racapé, V., Pierre, C., Metzl, N., Lo Monaco, C., Reverdin, G., Olsen, A., Morin, P., Vázquez-Rodríguez, M., Ríos, A. F., and Pérez, F. F.: Anthropogenic carbon changes in the Irminger Basin (1981–2006): Coupling δ13CDIC and DIC observations, Journal of Marine Systems, 126, 24–32, https://doi.org/10.1016/j.jmarsys.2012.12.005, 2013.

Rasmussen, C. E. and C. K. I. Williams. Gaussian Processes for Machine Learning. MIT Press. Cambridge, Massachusetts, 2006.

Regier, P., Duggan, M., Myers-Pigg, A., & Ward, N.: Effects of random forest modeling decisions on biogeochemical time series predictions. Limnology and Oceanography: Methods, 21(1), 40-52, https://doi.org/10.1002/lom3.10523, 2023.

Roobaert, A., Regnier, P., Landschützer, P., and Laruelle, G. G.: A novel sea surface pCO2 -product for the global coastal ocean resolving trends over 1982–2020, Earth Syst. Sci. Data, 16, 421–441, https://doi.org/10.5194/essd-16-421-2024, 2024.

Samanta, S., Dalai, T. K., Pattanaik, J. K., Rai, S. K., and Mazumdar, A.: Dissolved inorganic carbon (DIC) and its δ13C in the Ganga (Hooghly) River estuary, India: Evidence of DIC generation via organic carbon degradation and carbonate dissolution, Geochimica et Cosmochimica Acta, 165, 226–248, https://doi.org/10.1016/j.gca.2015.05.040, 2015.

Schmittner, A., Gruber, N., Mix, A. C., Key, R. M., Tagliabue, A., and Westberry, T. K.: Biology and air–sea gas exchange controls on the distribution of carbon isotope ratios (δ13C) in the ocean, Biogeosciences, 10, 5793–5816, https://doi.org/10.5194/bg-10-5793-2013, 2013.

Seeger M. Gaussian processes for machine learning. International journal of neural systems, 14(02): 69-106. https://doi.org/10.1142/S0129065704001899, 2004.

Sharp, J. D., Fassbender, A. J., Carter, B. R., Lavin, P. D., and Sutton, A. J.: A monthly surface pCO2 product for the California Current Large Marine Ecosystem, Earth Syst. Sci. Data, 14, 2081–2108, https://doi.org/10.5194/essd-14-2081-2022, 2022.

Silverman, B.W.: Density Estimation for Statistics and Data Analysis, Monographs on Statistics and Applied Probability, Chapman and Hall, London, UK, 1986.

Sonnerup, R. E. and Quay, P. D.: 13 C constraints on ocean carbon cycle models: 13 C IN OCEAN MODELS, Global Biogeochem. Cycles, 26, n/a-n/a, https://doi.org/10.1029/2010GB003980, 2012.

Su, J., Cai, W.-J., Hussain, N., Brodeur, J., Chen, B., and Huang, K.: Simultaneous determination of dissolved inorganic carbon (DIC) concentration and stable isotope (δ13C-DIC) by Cavity Ring-Down Spectroscopy: Application to study carbonate dynamics in the Chesapeake Bay, Marine Chemistry, 215, 103689, https://doi.org/10.1016/j.marchem.2019.103689, 2019.

Sun, Z., Li, X., Ouyang, Z., Featherstone, C., Atekwana, E. A., Hussain, N., and Cai, W.: Simultaneous onboard analysis of seawater dissolved inorganic carbon (DIC) concentration and stable isotope ratio (δ13 C-DIC), Limnology & Ocean Methods, 22, 862–875, https://doi.org/10.1002/lom3.10642, 2024.

Sun, Z., Gao, H., Dong, B., Hussain, N., Atekwana, E. A., and Cai, W.: High-resolution dataset of stable carbon isotope of dissolved inorganic carbon (δ13C-DIC) from the North Atlantic Ocean, Limnol Oceanogr Letters, lol2.70038, https://doi.org/10.1002/lol2.70038, 2025.

Tanhua, T., van Heuven, S., Key, R. M., Velo, A., Olsen, A., and Schirnick, C.: Quality control procedures and methods of the CARINA database, Earth Syst. Sci. Data 2: 35-49, https://doi.org/10.5194/essd-2-35-2010, 2010.

Taylor, J. R.: An introduction to error analysis: the study of uncertainties in physical measurements, 2nd ed., University Science Books, Sausalito, Calif, 327 pp., 1997.

Wanninkhof, R., Doney, S. C., Bullister, J. L., Levine, N. M., Warner, M., and Gruber, N.: Detecting anthropogenic CO2 changes in the interior Atlantic Ocean between 1989 and 2005, J. Geophys. Res., 115, 2010JC006251, https://doi.org/10.1029/2010JC006251, 2010.

Wu, Z., Lu, W., Roobaert, A., Song, L., Yan, X.-H., and Cai, W.-J.: A machine-learning reconstruction of sea surface p CO2 in the North American Atlantic Coastal Ocean Margin from 1993 to 2021, Earth Syst. Sci. Data, 17, 43–63, https://doi.org/10.5194/essd-17-43-2025, 2025.

Yang, B., Emerson, S. R., and Quay, P. D.: The Subtropical Ocean's Biological Carbon Pump Determined From O2 and DIC/DI 13 C Tracers, Geophys. Res. Lett., 46, 5361–5368, https://doi.org/10.1029/2018GL081239, 2019.